CZECH TECHNICAL UNIVERSITY IN PRAGUE
Faculty of Nuclear Sciences and Physical Engineering
Department of Physics

Bachelor's Thesis

Exclusive photoproduction of ψ(2S) vector mesons in lead-lead collisions in ALICE with Run2 data

Zuzana Gajdošová

Supervisor: doc. Jesús Guillermo Contreras Nuño, Ph.D.

Prague, 2017

ČESKÉ VYSOKÉ UČENÍ TECHNICKÉ
V PRAZE
Fakulta jaderná a fyzikálně inženýrská
Katedra fyziky

Bakalářska práce

Exkluzivní fotoprodukce vektorového mesonu ψ(2S) ve srážkach olovo - olovo na experimentu ALICE s daty z Run2

Zuzana Gajdošová

Vedoucí práce: doc. Jesús Guillermo Contreras Nuño, Ph.D.

Praha, 2017

Prohlášení

Prohlašuji, že jsem svou bakalářskou práci vypracovala samostatně a použila jsem pouze podklady (literaturu, projekty, SW atd.) uvedené v přiloženém seznamu.

Nemám závažný důvod proti použití tohoto školního díla ve smyslu §60 Zákona č.121/1200Sb., o právu autorském, o právech souvisejících s právem autorským a o změně některých zákonů (autorský zákon).

V Praze dne ....

Acknowledgements

I would like to express my gratitude to my supervisor, doc. Jesús Guillermo Contreras Nuño Ph.D., for his support, interest in my work, for his patience and bright advices, to my colleagues, specially Mgr. Michal Broz, Ph.D., for preparing the data sample and also for his valuable advices and answers to all my questions. I would like to give special thanks to my sister Katarína Gajdošová for her willingness to help and to my family and my boyfriend Javier Martínez Ruiz for their great support during my work.

Název práce: **Exkluzivní fotoprodukce vektorového mesonu ψ(2S) ve srážkach olovo - olovo na experimentu ALICE s daty z Run2**

Autor: Zuzana Gajdošová

Obor: Experimentální jaderná a částicová fyzika

Druh práce: Bakalářská práce

Vedoucí práce: doc. Jesús Guillermo Contreras Nuño, Ph.D.
Katedra fyziky, Fakulta jaderná a fyzikálně inženýrská,
České vysoké učení technické v Praze.

Abstrakt:

Na studium vnitřní struktury nukleonů je potřeba mít výkonný urychlovač, který by mohl srážet těžké ionty o energiích nekolik TeV. Studium tohoto typu srážek je prováděno na Velkém hadronovém urychlovači v CERNu při $\sqrt{s_{NN}} = 5.02$ TeV. Když nastane srážka při parametru dopadu větším než je součet poloměrů participujících těžkých iontů, nazývame tyto srážky srážkami Ultra-periferálními (UPC). Při tomto typu srážky jsou vyprodukovány pouze vektorové mezony, což nám poskytuje účinný nástroj pro studium jaderné gluonové distribuce při malém Bjorken(ově)-x. V této práci se zabývam speciálně exluzivní fotoprodukcí vektorového mezonu ψ(2S) ve střední rapiditě na detektoru ALICE s daty z Run2.

Klíčová slová: Ultra-periferální srážky, ALICE, ψ(2S)

Title: **Exclusive photoproduction of ψ(2S) vector mesons in lead-lead collisions in ALICE with Run2 data**

Author: Zuzana Gajdošová

Specialization: Experimental nuclear and particle physics

Supervisor: doc. Jesús Guillermo Contreras Nuño, Ph.D.
Department of physics, FacultyFaculty of Nuclear Sciences and Physical Engineering, Czech Technical University in Prague.

Abstract:

At the Large Hadron Collider (LHC), located at the CERN laboratory, we collide protons or heavy nuclei at large energies. The study of Pb–Pb collisions at $\sqrt{s_{NN}} = 5.02$ TeV can provide us with information about the internal structure of nucleons. When a collision occurs at impact parameters larger then the sum of the radii of the participant heavy ions, we call it an Ultra-peripheral collision (UPC). We study a special type of UPC, where only one vector meson is produced, which gives us a powerful tool to study the nuclear gluon distribution at low Bjorken-x. In this thesis, we study specifically the exclusive photoproduction of vector meson ψ(2S) at mid-rapidity at ALICE with Run2 data.

Keywords: Ultra-peripheral collisions, ALICE, ψ(2S)

Contents

1 Introduction **17**

2 Quarks and quarkonia **19**
2.1 Quarks . . . 19
2.2 Quarkonia . . . 20
2.2.1 The J/ψ, ψ(2S) and their discoveries . . . 20
2.2.2 Main ψ(2S) branching ratios . . . 22

3 Gluons and quantum chromodynamics **23**
3.1 DIS and structure functions . . . 23
3.2 Quantum chromodynamics . . . 25
3.2.1 Saturation . . . 26
3.2.2 Shadowing . . . 28

4 ALICE **31**
4.1 The origins of CERN . . . 31
4.2 The Large Hadron Collider . . . 31
4.3 The origins of ALICE . . . 34
4.4 ALICE . . . 35
4.4.1 Inner Tracking System . . . 35
4.4.2 Silicon Pixel Detector . . . 36
4.4.3 Silicon Drift Detector . . . 37
4.4.4 Silicon Strip Detector . . . 37
4.4.5 Time Projection Chamber . . . 38
4.4.6 Time of Flight . . . 40
4.4.7 V0 . . . 40
4.4.8 Zero-Degree Calorimeter . . . 42
4.4.9 The Diffractive detector . . . 43
4.5 The ALICE trigger system . . . 43
4.5.1 Online control system of ALICE . . . 43
4.5.2 Detector Control System . . . 44
4.5.3 Central Trigger Processor . . . 44
4.5.4 Data Acquisition . . . 45
4.5.5 High Level Trigger . . . 45
4.5.6 Data Quality Monitoring . . . 45
4.5.7 Detector Algorithms . . . 46
4.5.8 Offline Framework - Aliroot . . . 46
4.6 The GRID and LEGO trains . . . 46

5 Ultra-peripheral collisions **49**
5.1 Experimental observables of ψ(2S) 52

6 Previous measurements of charmonia in Pb-Pb UPC **55**
6.1 PHENIX measurement 55
6.2 Coherent and incoherent measurement of J/ψ at ALICE 55
6.3 Coherent measurement of ψ(2S) at ALICE 56
6.4 Coherent J/ψ cross section at the CMS 58

7 Analysis of the coherent ψ(2S) vector meson photoproduction with Run2 data **61**
7.1 Global event selection 61
7.1.1 Trigger CCUP8 61
7.1.2 Cut for bad runs 62
7.1.3 AD and V0 vetoes 62
7.1.4 Selection criteria using the ZDC 63
7.2 Selection criteria related to the interaction vertex 64
7.3 The selection of tracks 64
7.4 Invariant mass of ψ(2S) 67
7.5 Next steps 71

8 Summary and discusion **73**

List of Figures

2.1 The diagram of the charmonium family. Taken from [20]. 21

3.1 Scheme of deeply inelastic scattering (see text). 24
3.2 The momentum fraction of the quarks if quarks were free in the nucleon. . . 25
3.3 The momentum fraction of the quarks in the nucleon for not too small Bjorken-x. 26
3.4 The measured structure function of the proton at different virtualities Q^2 as a function of x (left) and the distribution of quarks and gluons (right) extracted from HERA. Note that the gluon distribution in the right has been scaled down by a factor of 20 so that it fits in the same scale as the valence-quark distributions. Taken from [31]. 27
3.5 The scheme of validity of different models with respect to virtuality and Bjorken-x. Taken from [40]. 27
3.6 The proton at smaller x contains a lot of partons (right), while at the same proton wave function but bigger x can be seen just free valence quarks (left). Taken from [47]. 28
3.7 The behaviour of the ratio $R^A_{F_2}$ as a function of the x at a given Q^2. Taken from [48]. 29

4.1 The signatures of the Swiss delegation in Paris. Taken from [51]. 32
4.2 The construction of CERN in Meyrin. Taken from [51]. 32
4.3 The sketch of LEP and LHC at CERN. Taken from [52]. 33
4.4 The diagram of the accelerator complex of CERN. Taken from [55]. 34
4.5 The poster from the Evian Meeting in 1992. Taken from [56]. 34
4.6 Status of the detector in 2012, taken from [60], with the AD detector modules superimposed in blue. 36
4.7 Sketch of ITS detector with its 6 layers [64]. 36
4.8 Left: Transverse cut of the SPD detector with 10 sectors carrying staves. Right: The carbon-fibre support sector with 6 staves. Taken from [65]. . . . 37
4.9 The transverse cut of the SDD module where cathodes can be seen. Taken from [65]. 38
4.10 The SDD and SSD ladder. Taken from [65]. 38
4.11 The schematic figure of the TPC. Taken from [67]. 39
4.12 Comparison of the energy loss dE/dx of determined particles in TPC at ALICE (left) with the energy loss in ITS at ALICE (right) [59]. 40
4.13 The measurement of particle identification provided by TOF at ALICE [68]. 41
4.14 Transverse cut of the ALICE detector, where ITS, TPC and TOF are depicted [69]. 41
4.15 The position of V0s detectors on a sketch of the part of ALICE detector [71]. 42
4.16 At the top is the schematic sketch of a V0A cell and at the bottom is a cell for the V0C with WLS fibres [72]. 42

4.17 Diagram of the process of a collision [73]. 43
4.18 The scheme of the layer of AD detector with WLS , hole for the beam pipe, scintillators pads and the support frame. Taken from AD note which is work in progress. 44
4.19 The scheme of DAQ. Taken from [58]. 45
4.20 The GRID infrastructure. Taken from [76]. 46

5.1 Diagram of an ultra-peripheral collision. The gradient of the colour represents the direction of movement of the Pb. 49
5.2 The illustration of the manner how the nuclei interact via the photons. . . . 50
5.3 Diagram for the coherent photoproduction off lead nuclei of a ψ(2S) vector and its subsequent decay into a J/ψ and two pions. 51
5.4 An event for coherent photoproduction of the ψ(2S) from PbPb collision in ALICE at $\sqrt{s_{NN}} = 2.76$ TeV from Run1. The red lines correspond to the $\mu^{\pm}$ and the yellow lines to the $\pi^{\pm}$. 51

6.1 The cross section of J/ψ production in Au-Au UPC at PHENIX. Taken from [77]. 56
6.2 Differential cross section of coherent J/ψ production compared to different theoretical models. Taken from [78]. 57
6.3 Differential cross section of incoherent J/ψ production compared to different theoretical models. Taken from [78]. 57
6.4 Differential cross section of ψ(2S) coherent production compared to different theoretical models. Taken from [80]. 58
6.5 The ratio of the coherent production cross section of J/ψ to ψ(2S). Taken from [80]. 59
6.6 The differential cross section of the J/ψ at CMS. Taken from [81]. 59

7.1 The V0, AD decisions after cuts 1 and 2, see Table 7.1. 63
7.2 The V0, AD correlations after cuts 1 and 2, see Table 7.1. 64
7.3 The ZDCA and ZDCC time after cuts 1, 2, 3a), 3b), 4a) and 4b), see Table 7.1. The green lines show the cut in ZDCC time, the red lines represent the cut in ZDCA time. Below is the correlation of ZDCA versus ZDCC time with these cuts depicted. 65
7.4 The ZDCA and ZDCC energy after cuts 1, 2, 3a), 3b), 4a), 4b), 5a-d), see Table 7.1. 66
7.5 (left) The SPD vertex contributors after using cuts 1, 2, 3a), 3b), 4a), 4b), 5a-d) and 6, see Table 7.1. (right) The distance between SPD vertex in z coordinate and primary vertex in z coordinate after using cuts 1, 2, 3a), 3b), 4a), 4b), 5a), 5b), 5c) and 5d), 6. The green lines represent the cut number 7 in Table 7.1. 66
7.6 The TPC PID of μ before cut 11 (up left) and after cuts 1-11 (up right) and TPC PID π before cut 12 (down left) and after cut 1-12 (down right), see Table 7.1. 68
7.7 The invariant mass of muon pairs (left) after cuts 1-14 and the p_T of this pair after cuts 1-14, see Table 7.1. 68
7.8 The invariant mass of ψ(2S) candidates (up left) and the mass vs. p_T of ψ(2S) (up right) after cuts 1-15, see Table 7.1. Below on the left is the coherent ψ(2S) yield and on the right is the mass of ψ(2S) vs. its p_T after cuts 1-16 from Table 7.1. 69

7.9 (up left) The invariant mass of ψ(2S) after cuts 1-17. (up right) The SPD vertex contributor after cuts 1-17. (Down left) the energy in ZDCA and (down right) the energy in ZDCC after cuts 1-17. For markers of cuts see Table 7.1. 70

List of Tables

2.1 Table of characteristics of quarks [15]. 20
2.2 Branching ratio of different ψ(2S) decay channels [20]. 22

7.1 Table of used cuts. 71

Chapter 1

Introduction

Already thinkers from ancient cultures wondered if matter was made of some fundamental elements, and if yes, which were they. This human curiosity have taken us from the idea of atoms, to experiments demonstrating their existence. And it has taken us beyond that, to discover that the atoms themselves are made of still more fundamental objects. They have a nucleus composed of nucleons, that is protons and neutrons. Nucleons are composed of quarks which are bound together by the glue called glouns. One of the main research topics today in fundamental physics is the study of quarks and gluons. All these phenomena are described by the theory called Quantum Chromodynamics (QCD).

This thesis will present a tool to study QCD: experiments in ultra-peripheral collision (UPC), which provide unique information about the gluon structure of nuclei and nucleons. In particular, this thesis presents the analysis of one type of UPC which produces only a $\psi(2S)$ meson, as measured with ALICE.

Chapter 2 presents quarks and quarkonia. In Chapter 3, gluons are added to the mix and results from deeply inelastic scattering are reported. Then QCD is discussed and two of the current areas of research, saturation and shadowing, are presented.

Chapter 4 presents ALICE and includes some historical remarks about the origins of CERN and of ALICE.

After presenting the functionality of the detecting system of the particles the thesis focuses in Chapter 5 and 6 on more details of UPC and some previous measurements in this field.

Chapter 7 presents the new results obtained in this thesis. Namely a first analysis of $\psi(2S)$ coherent photoproduction in Pb-Pb collisions at a centre-of-mass energy of 5.02 TeV.

Chapter 8 concludes this work with a summary and discussion of the results presented in the thesis and the next steps in this analysis.

Chapter 2

Quarks and quarkonia

By saying the word Nature everyone imagines something different: plants, animals, wind, sun, planets, etc. According to our current understanding, there are just a few building blocks underlying all these phenomena.

Bohr's atomic model (1913) [1, 2] divides the atom in negative charged electrons travelling in orbits around a small positive charged nucleus. After this model was proposed, many years passed developing theories and providing experiments until in 1932 Chadwick discovered the neutron [3].

A long list of experiments, from those at SLAC at the end of the 60's and beginning of the 70's to those of HERA from 1992 to 2007, have revealed that the protons and neutrons, believed in the past to be elementary, have an internal structure. This structure consists of partons which is the common name for quarks and gluons.

2.1 Quarks

Murray Gell-Mann is the name of the American physicist who called the entities forming protons and neutrons quarks [4]. Nowadays six different types of quarks are known. They are classified according to their properties. Every quark has an original *flavour*: *up, down, strange, charm, top, bottom.* The *up* and *down* quarks were named according to the orientation of their isospin. The discovery of the K particle [5] forced the introduction of a new quantum number: the K lifetime was inordinately long which at that time seemed *strange* so the new quantum number received this name and later was related to the strange quarks. Shortly after Gell-Mann proposal, the possibility of a fourth quark, which was named *charm*, was explored [6]. A strong theoretical argument for the need of the charm quark was given by the GIM mechanism [7]. Finally it was discovered, during the so-called November revolution, simultaneously in two laboratories [8, 9]. Later on, two other quarks, with similar characteristics as the up and down quarks, were discovered [10, 11, 12]. For this reason they were named *top* and *bottom*.

Just like protons, electrons etc., quarks have its own antiparticle [13, 14]. Quarks have never been seen free in Nature. Their existence was proposed by Gell-Mann in 1964 as a means to organize the numerous particles found up to then. In his model, the quantum numbers of strongly-interacting particles are carried either by three quakrs in so-called baryons or by a quark and an antiquark in so-called mesons. As baryons are assigned a baryon quantum number of 1, then quarks have a baryon number of 1/3.

Relating the charge to isospin and baryon number it was observed that quarks carry fractional electronic charge either 2/3 or $-1/3$. It is known that the baryons are fermions, which in other words means that those particles have half-integer spin and that the mesons are bosons, i.e. they have integer spin.

Flavour	q	Charge Q	Spin S	Isospin I_3	Mass M [MeV]
up	u	$\frac{2}{3}$e	$\frac{1}{2}$	$+\frac{1}{2}$	$M_u = 2.3^{+0.7}_{-0.5}$
down	d	$-\frac{1}{3}$e	$\frac{1}{2}$	$-\frac{1}{2}$	$M_d = 4.8^{+0.5}_{-0.3}$
strange	s	$-\frac{1}{3}$e	$\frac{1}{2}$	0	$M_s = 95 \pm 5$
charm	c	$\frac{2}{3}$e	$\frac{1}{2}$	0	$M_c = 1275 \pm 25$
bottom	b	$-\frac{1}{3}$e	$\frac{1}{2}$	0	$M_b = 4180 \pm 30$
top	t	$\frac{2}{3}$e	$\frac{1}{2}$	0	$M_t = 173210 \pm 510 \pm 710$

Table 2.1: Table of characteristics of quarks [15].

It seemed that quarks provided a good description of particles until the discovery of the Ω^- particle [16], which in Gell-Mann model is formed by three strange quarks. As quarks are fermions, they are subjected to Pauli's exclusion principle [17, 18], so three of them could not form a particle in the ground state. The answer to this puzzle was the introduction of another quantum number labelled as *colour* [19]. This name can be explained with the analogy of light. Since the unity of the blue, red and green colour produces white - neutral-light so baryons containing the three quark colours must be neutral. On the other hand there are mesons which have just two constituents, the $\bar{q}q$ pair. The neutrality of the colour can be reached by combining the same type of the colour and its anticolour.

The recapitulation of the quantum numbers of the quarks is depicted in Table 2.1.

2.2 Quarkonia

A particle formed of a heavy quark and an anti-quark of the same flavour in a bounded colourless state is called quarkonia. We distinguish between several types of quarkonia according to their flavour. Charmonia are the bounded state of $c\bar{c}$ and analogously the bounded states of $b\bar{b}$ is called bottomium. Then there are quarkonia which have no specific name like that formed from u-quarks, d-quarks and s-quarks. There is no convention to call the bounded formation of these lighter quarks as quarkonium. The top quarks have, as seen in Table 2.1, a large mass, which implies that the bounded state of such quarks cannot exist.

In this thesis, we will discuss some aspects of the measurement of a particular charmonium state, the ψ(2S), in coherent photoproduction. In this case, charmonia can be used as a tool to study the structure of lead nucleus, specifically an effect called shadowing, which will be introduced later on in Sec. 3.2.

Besides the mentioned ψ(2S) there are other charmonium, e.g. $\eta(1S)$, $\chi_{c0}(1P)$, $h_c(1P)$, etc. and probably the most familiar J/ψ, see Figure 2.1.

2.2.1 The J/ψ, ψ(2S) and their discoveries

Behind the discovery of the vector meson J/ψ stand two names: Samuel Ting and Burton Richter. Each scientist studied this particle at a different experiment and by a different method. Richter with his team observed the J/ψ with the experiment SPEAR at the Stanford Linear Accelerator Center, SLAC-LBL, in a process of electron-positron collisions producing hadrons [9], while Ting studied this particle at the Brookhaven National Laboratory by shooting protons against a beryllium target obtaining leptons [10].

On November 11, 1974 both physicists announced the discovery of a new resonance, nowadays known by the name J/ψ, J as Samuel Ting wanted to call it and ψ the name

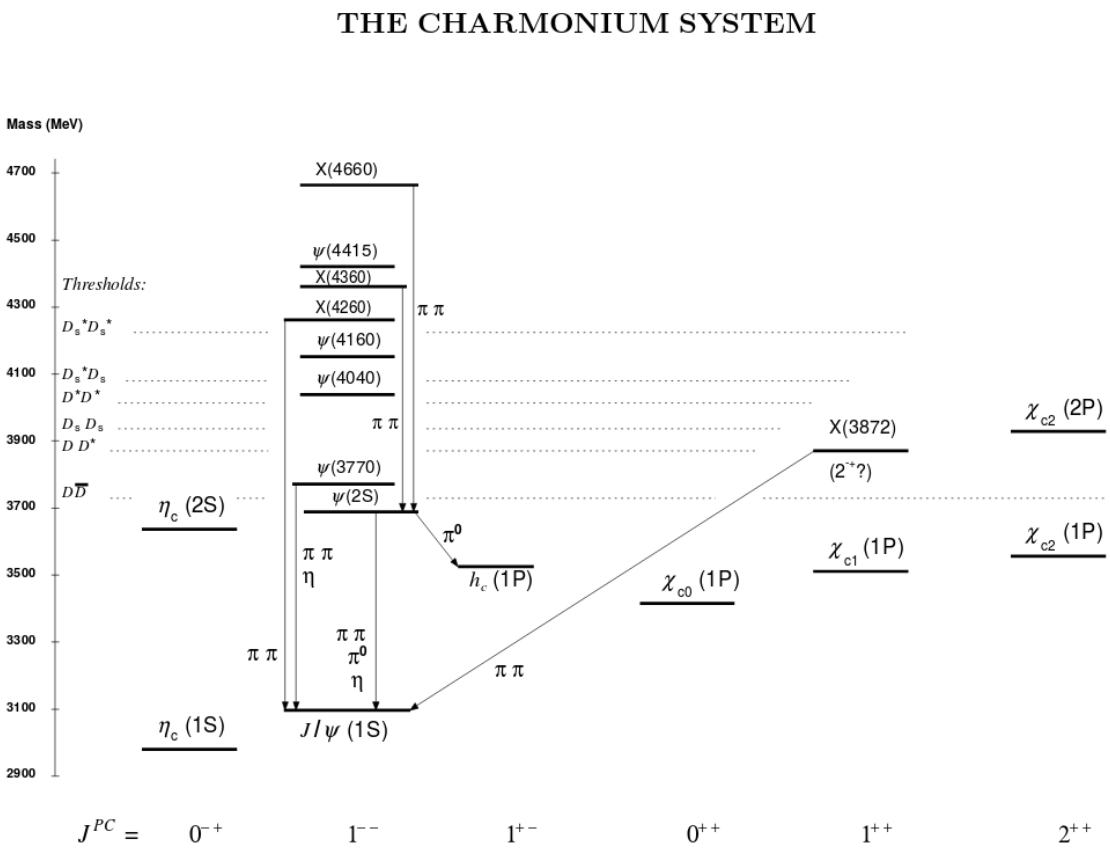

Figure 2.1: The diagram of the charmonium family. Taken from [20].

chosen by Burton Richter. The current value for the mass of the J/ψ is (3096.916 ± 0.011) MeV/c^2 [20].

Once the J/ψ was discovered, Richter decided to search more for another charmonium instead of continuing to study deeply the J/ψ. The three of them, Burton Richter, Ewan Peterson and Robert Melmen, decided to put SPEAR in a "scanning mode", which means increasing the energy of the collision every three minutes in intervals of 1 MeV. They decided to start at a centre-of-mass energy of 3.6 GeV [8].

On November 25, 1974 the new particle $\psi(3695)$ was discovered: First SPEAR was tested by scanning over the J/ψ particle at an energy of 3.1 GeV. The next day a run began at higher energies. When the bump was spotted, the run was stopped and the velocity of scanning was reduced. The energy was decreased to 3.69 GeV. The mass of the new particle was given to $m_{\psi(3695)} = (3.695 \pm 0.004)$ GeV. Since then the mass of the ψ(2S) was constrained to the current value of $3686.109^{+0.012}_{-0.014}$ MeV/c^2 and its full width is $\Gamma = (299 \pm 8)$ keV [20].

2.2.2 Main ψ(2S) branching ratios

In this thesis the production of ψ(2S) is used as a tool to understand some aspects of the high energy limit of QCD. The ψ(2S) can be measured in different decay channels. It can decay directly into two leptons $\psi(2S) \to l^- l^+$. Another frequently used channel is the channel where the final state consist of four particles, $\psi(2S) \to J/\psi + \pi^-\pi^+$, where $J/\psi \to l^- l^+$. In this thesis we study the former decay with the J/ψ decaying into leptons, for the case where the lepton l is a muon. The corresponding decay channels are reported in Table 2.2.

Decay channel	Branching ratio
$\psi(2S) \to J/\psi + \pi^-\pi^+$	$34.00\% \pm 0.40\%$
$J/\psi \to \mu^- + \mu^+$	$5.93\% \pm 0.06\%$
$J/\psi \to e^- + e^+$	$5.94\% \pm 0.06\%$

Table 2.2: Branching ratio of different ψ(2S) decay channels [20].

Chapter 3

Gluons and quantum chromodynamics

One of the main objects of study in contemporary high-energy physics is the structure of hadrons (baryons and mesons) and deeply inelastic scattering (DIS) is one of the best tools to study the dynamics of nucleon structure. In DIS a high-energy probe, normally an electron or a muon, is scattered off the hadronic target.

At high energy the so-called probes, electron or muon, are scattered off the target, e.g. a proton. The interaction between the lepton and the target is mediated in leading order by a single photon exchange. When the photon is virtual, this process is called electroproduction and when the photon is (quasi-)real is called photoproduction.

In fact in this thesis we will be interested in the case of photoproduction when the target is not a nucleon but a heavy ion, specifically a lead (Pb) nucleus. All these concepts will be discussed in this section starting with DIS, then its relation to QCD and then saturation and shadowing.

3.1 DIS and structure functions

The minimum momentum of a lepton to be able to scatter off a nucleon can be derived from the simple formula $p\lambda = h$. As it is known that the diameter of the nucleon is 10^{-15} m [21], the previous formula yields p as above 1 GeV/c. To observe any structure the wavelength of the probe must be smaller than the diameter of the nucleon which means momenta larger than 1 GeV/c.

To understand how DIS works we must first define some kinematic variables which are the energy loss of the lepton in this process:

$$\nu = E_i - E_f, \tag{3.1}$$

where E_i is the initial energy and E_f the final energy, and the momentum transferred Q^2 of the lepton [22]:

$$Q^2 = 2E_iE_f(1 - \cos\theta), \tag{3.2}$$

where θ is the polar angle of the scattered lepton.

After defining the kinematics the first step is to divide the electroproduction process into three parts as seen in Figure 3.1. The lepton current and the propagation of the single photon, parts a) and b), are electromagnetic processes, well known from QED. The problem is in describing mathematically the hadron current, the part c). It is known that

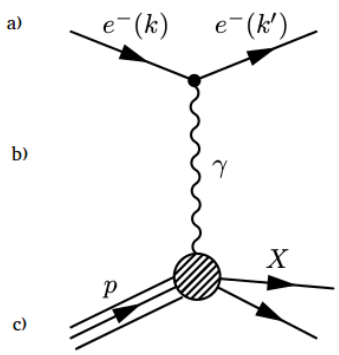

Figure 3.1: Scheme of deeply inelastic scattering (see text).

the hadronic current involved in this process has to be a vector current. As this current is defined at the level of the amplitude, it should give origin to a tensor object at the level of the cross section. This tensor incorporates the general conservation laws to be respected by the interaction and describes the internal structure of the nucleon. When Q^2 is not too large and effects of the weak interaction can be neglected, the structure of the hadron can be described with only two so-called *structure functions* $F_1(Q^2, \nu)$, $F_2(Q^2, \nu)$.

In this case, the differential cross-section for electron nucleon scattering is:

$$\frac{\mathrm{d}^2\sigma}{\mathrm{dQ}^2\mathrm{d}\nu} = \frac{4\pi\alpha^2}{Q^4}\frac{E_f}{E_i M_p}\left(\frac{M_p}{\nu}F_2(Q^2,\nu)\cos^2\frac{\theta}{2} + 2F_1(Q^2,\nu)\sin^2\frac{\theta}{2}\right). \tag{3.3}$$

Structure functions are dimensionless, however they depend on dimension-full magnitudes ν and Q^2. Let's consider for a moment the case of elastic scattering, where we find that the relation between the energy loss ν and the momentum transfer Q^2 in the low-energy elastic scattering is $Q^2 = 2\nu M_N$. The conclusion is that the dimensionality must be cancelled out between Q^2 and ν to obtain a dimensionless structure function. But our interest is focused on DIS at high energies since in this case the lepton probes the internal structure of the nucleon. This means that we will be interested in the case when $\nu, Q^2 \to \infty$. At such energies the wavelength of the photon is so small that speaking about the presence of the whole nucleon makes no sense which implies that the scaling of DIS in the structure functions by the mass of the whole nucleon does not have any sense.

James Bjorken resolved this problem in DIS [23] by introducing the dimensionless ratio depending on these two observables:

$$x = \frac{Q^2}{2\nu M_N}. \tag{3.4}$$

Thus in the case where the energy loss and the momentum transfer are asymptotically approaching infinity, the structure functions no more depends on Q^2 and ν but on Bjorken-x, $F_{1,2}^{e,N}(x)$, the so-called Bjorken scaling.

Furthermore, Bjorken presented a model where the nucleons were made of point like constituents [24] which he identified with the partons proposed by Feynman [25]. For the case where these partons have spin $\frac{1}{2}$ the structure functions $F_1(x)$ and $F_2(x)$ are related by $2xF_1(x) = F_2(x)$, which is called the Callan-Gross relation [26], thus if the ratio $2xF_1(x)/F_2(x) = 1$ the partons must have spin $\frac{1}{2}$. Experimentally was indeed observed this phenomenon for Bjorken-$x \geq 0.2$ [26]. These results demonstrated that nucleons are

not elementary particles, but have an internal structure and that part of that structure is given by spin $\frac{1}{2}$ particles that were related to the quarks proposed by Gell-Mann.

Further DIS experiments demonstrated that the fraction of the momentum of the proton carried by the quarks was just about one half. So there had to be something else in the proton. There is no doubt that to understand more the structure of the, once-upon-a-time elementary, hadrons it is necessary to go beyond a theory of quarks and include gluons as proposed in 1973 by Fritzch, Gell-Mann and Leutwyler [27] and made possible with the discovery of asymptotic freedom [28, 29].

3.2 Quantum chromodynamics

Deeply inelastic scattering as described above was done under the assumption of the target being at rest. It is necessary to stress this since the interpretation of the model is frame dependent. This choice was natural at the time of the proposals by Bjorken, when the experiments were performed under these conditions. To date, the only exceptions have been the experiments at the HERA collider (1992-2007 [30]).

From the previous section we know that the nucleons are composed of partons. Now DIS offers another question: Are these quarks inside the nucleon free or are bound together by something else?

If they were free, every quark inside the nucleon would bear the exact same fraction of the momentum of the whole nucleon. As the quark model requires the proton to carry the quantum numbers of three quarks (uud), then as seen in Figure 3.2, each quark would carry one third of the momentum; i.e. $x = \frac{1}{3}$. The fraction of the momentum of the parton is said Bjorken-x, $x = \frac{p_{parton}}{p_{nucleon}}$.

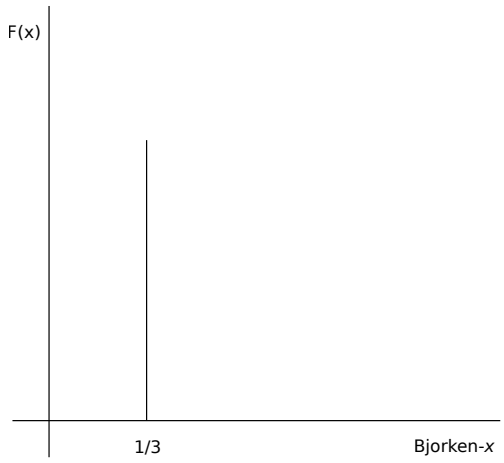

Figure 3.2: The momentum fraction of the quarks if quarks were free in the nucleon.

However experiments show something different. The nice δ function is not observed. At relatively large values of x, the behaviour is as shown in Figure 3.3. Experiment reveals that quarks are not free inside the nucleon and that they are bound together by the strong force and interact with each other through other partons called gluons which are responsible for the "missing" fraction of the momentum of the proton.

When the probe which is something like a microscope approaches the nucleon with the wavelength $\approx 10^{-17}$ m, it sees free quarks. But with increasing distance between quarks the strength of the binding also increases. This observation is contrary to the known behaviour of the electromagnetic force. Approaching from the infinity to an electron the whole charge can not be observed nor can be reached as a consequence of the repulsion or the strengthen of the electromagnetic force. In the case of QCD, with decreasing distance the interquark forces also decrease until the point where they seem to be free. The phenomenon is called the *asymptotic freedom* [28, 29].

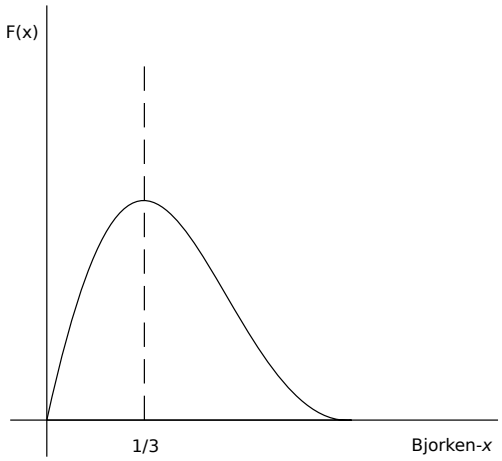

Figure 3.3: The momentum fraction of the quarks in the nucleon for not too small Bjorken-x.

On the other hand there is a *quark confinement* which is responsible for the fact that free quarks have not been observed. With high momentum of the probe, the target breaks which would mean that some quark would be shot out of the proton - target. But the experiments show that the parton which is kicked out, forms new hadrons, so we cannot observe free quarks.

Modern experiments show a complex partonic structure of the proton; this is seen in Figure 3.4, which shows the current F_2 data and the corresponding distribution of quarks and gluons as extracted from HERA data using perturbative QCD [31]. It is seen that for small values of Bjorken-x the structure of the proton is dominated by gluons.

3.2.1 Saturation

The extraction of the parton distributions shown in Figure 3.4 (right) were performed using so-called evolution equations. These are integro-differential equations obtained from a perturbative expansion of QCD. There are different ways of doing this perturbative expansion. The most common are DGLAP [32, 33, 34] and BFKL [35, 36, 37, 38, 39]. The two of them describe parton distribution functions (PDF) at different Bjorken-x. Both required a large energy scale to be applicable. In the case of DIS, this translate in the requirement of having a minimum virtuality Q^2 of a few GeV^2 then DGLAP is applied and allows to find the PDF for $Q^2 > Q_0^2$ at all x, where Q_0^2 is the scale at which the initial condition is given. DGLAP is valid for not so small values of x, because it neglects some

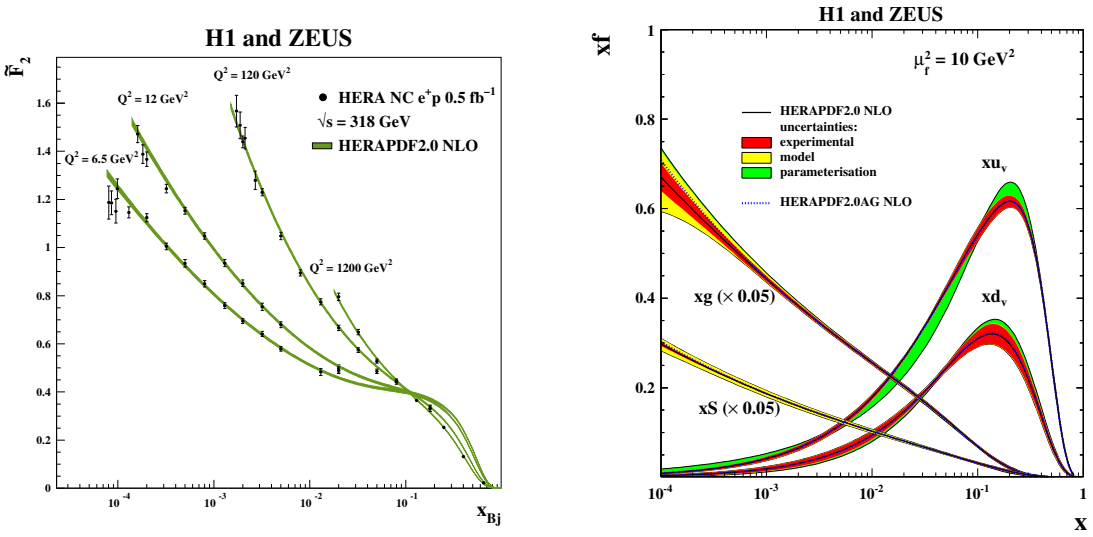

Figure 3.4: The measured structure function of the proton at different virtualities Q^2 as a function of x (left) and the distribution of quarks and gluons (right) extracted from HERA. Note that the gluon distribution in the right has been scaled down by a factor of 20 so that it fits in the same scale as the valence-quark distributions. Taken from [31].

terms proportional to $\ln(1/x)$. On the other hand, BFKL represents the change of the structure function in $\ln(1/x)$ at a fixed resolution Q^2. These different regimes are shown in the Figure 3.5. At low Q^2 is confinement, than there is the linear regime of these two evolution equations. This region is called *low density* and it could help to imagine it if we take a look at the Figure 3.6 left.

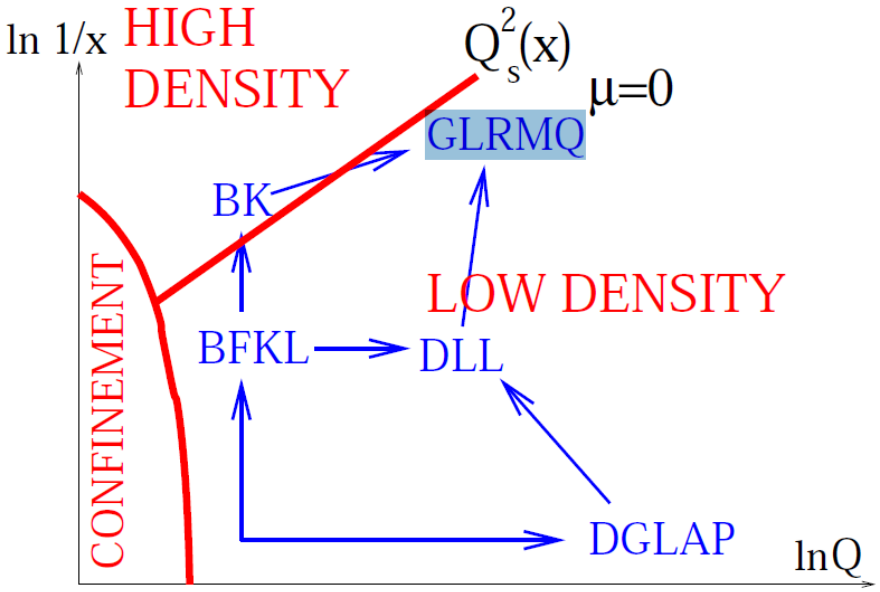

Figure 3.5: The scheme of validity of different models with respect to virtuality and Bjorken-x. Taken from [40].

With decreasing x what in another words means increasing energy, the probe will "see"

a lot of partons, sea quarks and gluons in the nucleon. The appearance of new and new partons cannot last forever, the hadron gets saturated, meaning that the assumptions behind perturbative QCD (namely that, due to asymptotic freedom, and the high energy of the interaction, the partons can be considered quasi-free during the scattering) are not any more valid and a new set of equations, incorporating non-linear effects are needed. One such type of equations are the BK equations [41, 42, 43, 44, 45, 46]. Figure 3.5 shows a line $Q_s(x)$ the so-called saturation scale which separates the region where DGLAP and BFKL are valid, from the region where saturation effects are important. The exact location of this saturation line is not known experimentally nor predicted by theory. One of the main topics of research nowadays in perturbative QCD is the location of this saturation line.

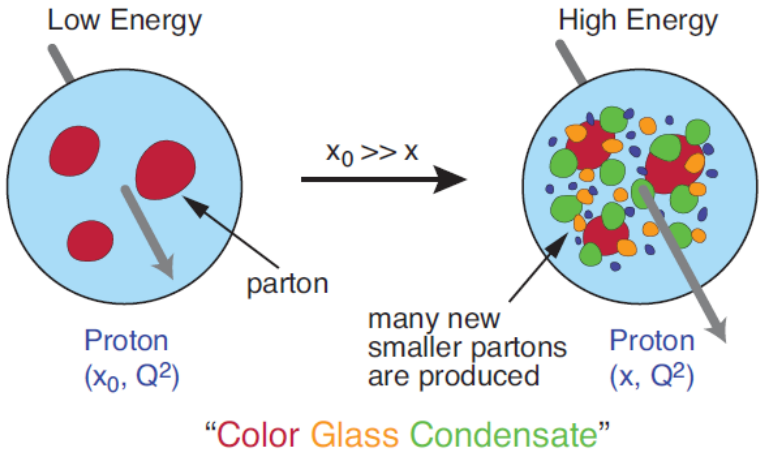

Figure 3.6: The proton at smaller x contains a lot of partons (right), while at the same proton wave function but bigger x can be seen just free valence quarks (left). Taken from [47].

3.2.2 Shadowing

A nuclear phenomenon studied at low Bjorken-x and small or moderate Q^2 is called *Shadowing* [48]. As it was mentioned above, the shape and structure of the nucleons is described by the structure functions. Thus, one could suppose that the nuclear structure function is the sum of the structure functions of their nucleons. Surprisingly it is not. Nuclear structure functions are quantified by the ratio:

$$R^A_{F_2}(x, Q^2) = \frac{F_2^A(x, Q^2)}{AF_2^{nucleon}(x, Q^2)}, \tag{3.5}$$

where x is the Bjorken-x, Q^2 in DIS is the virtuality of the incoming photon or in other words the resolution of the probe, A is the number of nucleons in the nucleus and F_2 is the structure function.

One would suppose that this ratio is equal to 1, but from the experiments, the fact is that is less than 1 for small values of x. The behaviour of the ratio from the Eq. (3.5) can be divided into four region as shown in Figure 3.7.

The Fermi motion can be seen for $R^A_{F_2} > 1$ and for $x > 0.8$. The second region is the region $0.3 < x < 0.8$ and $R^A_{F_2} < 1$. This region is called EMC, the name derived from European Muon Collaboration, which was the first to observe this [49]. The third region is where $R^A_{F_2}$ is again greater than 1 for $0.1 < x < 0.3$, the so-called antishadowing region,

where one sees the effect of conservation laws. The fourth region the so-called shadowing region, where $R^A_{F_2} < 1$ and it is observed for Bjorken-$x < 0.1$ [48].

From the above we can sum up that shadowing can be observable at small x, the smaller the value of x the greater it is shadowing. Shadowing also grows with A. Shadowing could be caused by quarks or by gluons or by both of them. In this thesis, we study a process that is specially sensitive to the contribution of gluons to shadowing in Pb nuclei at small x.

There are also predictions that shadowing depends on the impact parameter (for the most recent prediction in this direction see [50]), but until now no experimental information is available.

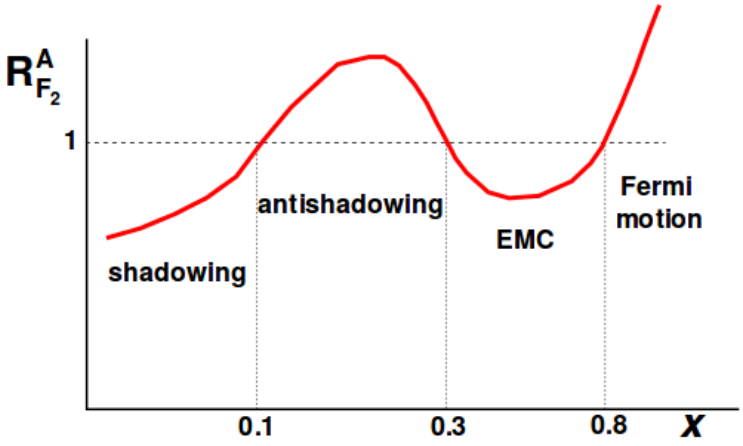

Figure 3.7: The behaviour of the ratio $R^A_{F_2}$ as a function of the x at a given Q^2. Taken from [48].

Until this point we were speaking about DIS where the highly virtual photon interacted with one nucleon. In this thesis we are interested in quasi-real photoproduction. The reason why DIS requires a photon with high virtuality is to have a large energy scale, in DIS case the photon virtuality, that allows to use perturbation theory. In the process we are interested in this thesis, the photon is quasi-real, and the large energy scale is given by the mass of the charm quark.

Chapter 4

ALICE

4.1 The origins of CERN

Studying Nature and understanding the origin of the Universe goes in one direction with technical development and requires a cooperation between scientists. This fact was realized more than 60 years ago and from it came the idea of establish a centre for nuclear research and astrophysics in Europe after the war. This centre is known today as CERN.

Denis de Rougemont met Albert Einstein in 1947. They discussed the idea to link the European Union and mastering nuclear physics. Two years later this idea was presented in *Conference on Culture* in December 1949 in Lausanne.

In 1952 The Tribune of Geneva presented the arguments which were in favour for the establishment of such centre of physics in Switzerland, in Geneva, with respect to other candidates like Copenhagen, Paris and Amsterdam. The main reasons were: important scientific heritage, highly specialized manpower, small country, available electric power, suitable place to live, education for children of scientists, neutrality which would ensure that the research would be exclusively for the peaceful purposes, etc. [51].

However the communist party was opposed to the whole idea and a campaign against CERN took place, fortunately it was repelled. Two days after the communist campaign, 1st of July 1953 the Swiss delegation signed in Paris the Convention for the establishment of CERN, see Figure 4.1. Now it had to be ratified by twelve countries [51].

On May 17th 1954 CERN was born. The construction took place on the Meyrin site, see Figure 4.2. In September 29, after ratification of 12 states also France and Germany ratified the Convention which meant that CERN officially started.

Since its origin there have been a series of accelerators in operation at CERN. Each larger in some sense that its predecessors. In 1989 the Large Electron-Positron Collider (LEP) started operation with its 27 km in diameter and with its main experiments: ALEPH, DELPHI, OPAL and L3. LEP had a big role in shaping the Standard Model. LEP was closed down in 2000. LEP was substituted by a new collider, the Large Hadron Collider (LHC) which begun to operate in 2009. Its main experiments are: CMS, ATLAS, LHCb and ALICE.

4.2 The Large Hadron Collider

The Large Hadron Collider (LHC) at CERN is situated between 45 to 170 m underground in the same tunnel and slightly above where LEP was located, Figure 4.3.

The LHC is located in a circular tunnel 27 km long. It can accelerate beams of protons (p) and of lead ions (Pb) and made them collide in pp, p-Pb and Pb-Pb modes at different

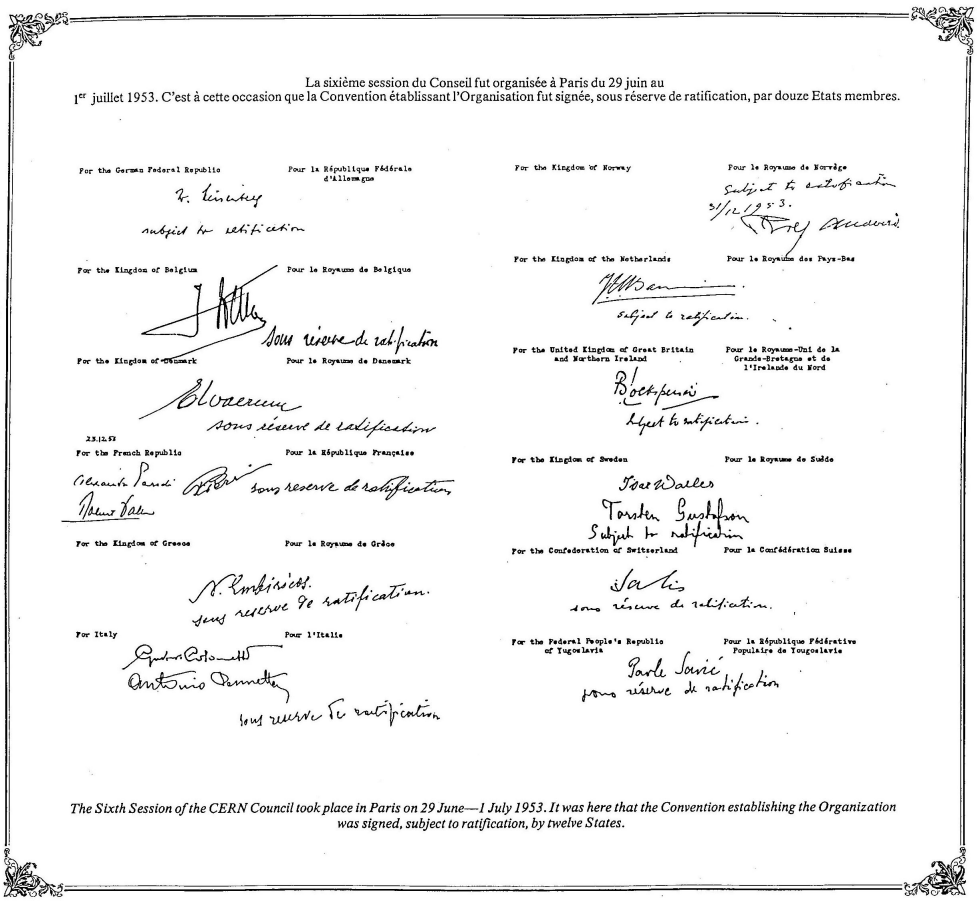

La sixième session du Conseil fut organisée à Paris du 29 juin au 1er juillet 1953. C'est à cette occasion que la Convention établissant l'Organisation fut signée, sous réserve de ratification, par douze Etats membres.

For the German Federal Republic — Pour la République Fédérale d'Allemagne
subject to ratification

For the Kingdom of Belgium — Pour le Royaume de Belgique
sous réserve de ratification

For the Kingdom of Denmark — Pour le Royaume de Danemark
23.12.53
sous réserve de ratification

For the French Republic — Pour la République Française
sous reserve de ratification

For the Kingdom of Greece — Pour le Royaume de Grèce
sous reserve de ratification.

For Italy — Pour l'Italie
sous reserve de ratification

For the Kingdom of Norway — Pour le Royaume de Norvège
Subject to ratification
31/12/1953

For the Kingdom of the Netherlands — Pour le Royaume des Pays-Bas
subject to ratification.

For the United Kingdom of Great Britain and Northern Ireland — Pour le Royaume-Uni de la Grande-Bretagne et de l'Irelande du Nord
Subject to ratification.

For the Kingdom of Sweden — Pour le Royaume de Suède
Subject to ratification

For the Confederation of Switzerland — Pour la Confédération Suisse
sous réserve de ratification.

For the Federal People's Republic of Yugoslavia — Pour la République Fédérative Populaire de Yougoslavie
sous réserve de ratification

The Sixth Session of the CERN Council took place in Paris on 29 June—1 July 1953. It was here that the Convention establishing the Organization was signed, subject to ratification, by twelve States.

Figure 4.1: The signatures of the Swiss delegation in Paris. Taken from [51].

Figure 4.2: The construction of CERN in Meyrin. Taken from [51].

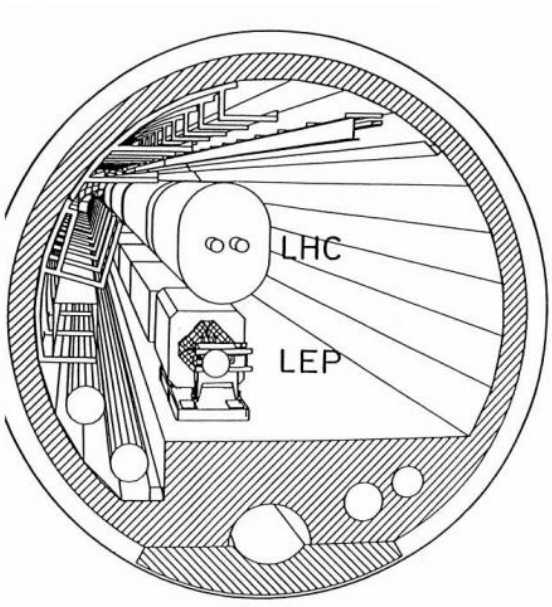

Figure 4.3: The sketch of LEP and LHC at CERN. Taken from [52].

centre-of-mass energies. These beams are accelerated to a velocity near that of light (99.999991 %) in two opposite counter-rotating beam pipes. The design collision energy is $\sqrt{s} = 14$ TeV for pp and for Pb-Pb is $\sqrt{s} = 5.5$ TeV. One proton beam contains up to 2808 bunches and each bunch contains some 1.15×10^{11} protons. One lead beam contains 600 bunches, each of 7×10^7 lead ions [53]. Before the moment of the collision, beams must pass through the process of injection and acceleration through different smaller accelerators.

The ions of Pb are extracted from a sample of high purity lead. This sample is than warmed up to 550°C. The vapour of lead is ionised by a current of electrons. The ions are then accelerated to an energy of 4.2 MeV/u per nucleon. Then the process continues by passing these ions through a carbon foil in order to constrain the beam and obtain the ion of Pb. These ions are then conducted to the Low Energy Ion Ring (LEIR) and are accelerated to an energy of 72 MeV/u. From LEIR the ions go to the PS where they are accelerated even more and again pass the carbon foil which is the point where the pure nuclei of the Pb^{82+} are obtained and are sent to the SPS to accelerate them to the energy of 177 GeV/u. Now the ions are prepared to enter the LHC, see Figure 4.4, and to be accelerated so that they collide at an energy of $\sqrt{s} = 5.5$ TeV. In Run1 this energy was significantly lower $\sqrt{s} = 2.76$ TeV [54].

A similar but simpler process is done for protons. Protons are obtained from a bottle of hydrogen where the electrons are put away. After reaching pure protons these are sent to the linear accelerator Linac2 and reach the energy of 50 MeV, then are sent to the Proton Synchrotron Booster (PSB). After that the beam continues to the PS and than to the SPS. The protons after reaching the SPS are accelerated to an energy of 450 GeV/u and injected to the LHC where they reach the final design energy of 7 TeV [54], see Figure 4.4.

All this process from obtaining the pure ions and the protons to the collision last some 20 minutes. The time between consecutive bunches in a beam is 25 ns which represents a maximum collision frequency of 400 MHz.

To get beams to travel in circuits they must be bend by a magnetic field of 8.3 T produced by superconducting dipole magnets. These dipole magnets are made of niob-titan (NbTi) cables which are cooled down by liquid helium to a temperature of 1.9

K (-273.1°C). At this temperature the cables are superconducting and reach an electric current of 11700 A.

To get the protons or ions to travel in the beams they must be focused by quadrupole magnets. In total the LHC contains 9600 magnets which include the already mentioned dipole and quadrupole magnets and also sextupole, octupole, decupole etc. The beams can collide in 8 intersect points. One of these point is point 2, where the ALICE detector is situated, see Figure 4.4 [54].

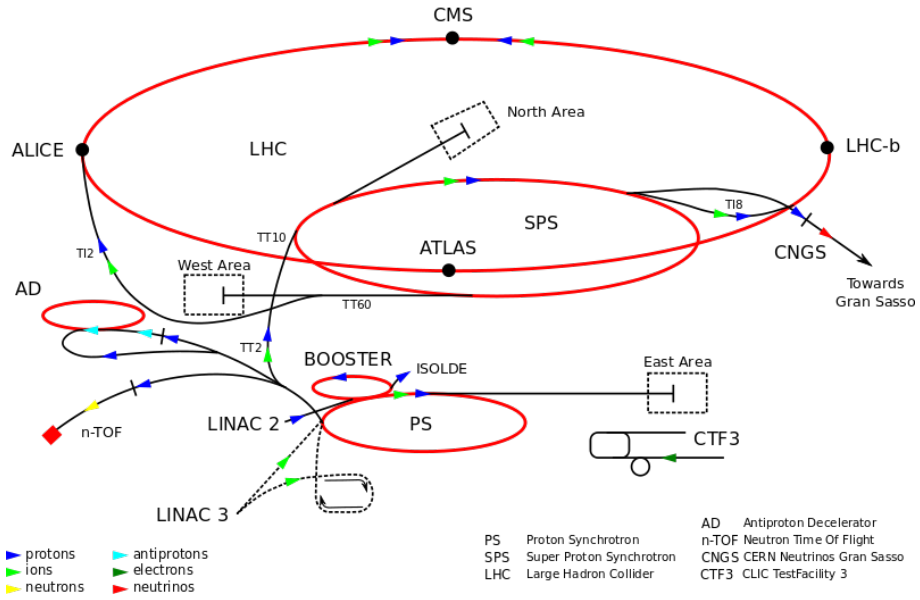

Figure 4.4: The diagram of the accelerator complex of CERN. Taken from [55].

4.3 The origins of ALICE

The first discussions to have a program of heavy ion physics at the LHC began in 1986. From then, the first concept of a detector, and the collaboration to design and build it was born. These ideas were submitted in 1992 in the famous Evian-les-Bains Meeting *Towards the LHC experimental programme*, see Figure 4.5.

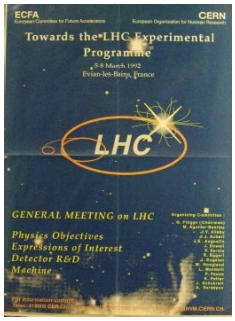

Figure 4.5: The poster from the Evian Meeting in 1992. Taken from [56].

Jurgen Schukraft was one of the leaders behind this idea and later on acted many years as ALICE spokesperson. The original design of the ALICE detector was not the same as we know today. It passed through some development. Hans H. Gutbrod proposed the idea of a large solenoid magnet, where every part of the subdetectors would be enclosed. For

this purpose was suitable the magnet from the LEP experiment L3, although it needed an upgrade which was done by Sam Ting. After that in 1993 the concept of the detector was proposed and it was named A Large Ion Collider Experiment ALICE [56].

In 1995 a technical design was submitted demonstrating that ALICE will be able to measure the phase-space distribution, that it will be sensitive to observables like photons, electrons, muons and hadrons. In 1997 the project ALICE was approved.

In 2001 the L3 experiment was dismantled at LEP and in 2002 ALICE developed the ALICE production environment (AliEn). After 2002 the Inner Tracking System (ITS), Zero Degree Calorimeter (ZDC), Time Projection Chamber (TPC), Time of Flight (TOF) and Transition Radiation Detector (TRD) systems were installed in the large cylindrical construction of the L3 experiment.

In June 16, 2006 ALICE detected the first real events in TPC. This events were tracks of cosmic rays [57].

One year later, the Central Trigger Processor (CTP) was installed. From then on, and until 2009 ALICE was preparing for its first operation. Finally in 2009 LHC begun its first run and ALICE saw its first collision.

4.4 ALICE

One of the four main experiments at the LHC is ALICE. With a weight of 10000 tonnes, 16 meters in height, 16 meters in width and 26 meters in length is a large complex detector suitable to study the Quark Gluon Plasma; a state of matter which existed shortly after the Big Bang and which is now created in heavy-ion collisions at the LHC. ALICE was designed to withstand a high particle multiplicity environment. The detector ALICE is designed to measure hadrons, electrons, muons, photons produced in the collisions down to very low transverse momentum ≈ 0.1 GeV. It uses a large array of techniques of particle identification (PID).

The detector is composed of two main parts: central barrel and forward muon spectrometer. The central barrel is enclosed in the L3 solenoid magnet with a magnetic field of 0.5 T and covers the pseudorapidity of $|\eta| \leq 0.9$. The forward muon spectrometer with its dipole magnets provides an integrated field of 3 T. There is a detector, composed of 60 modules of plastic scintillators, situated on the top of the central barrel called ACORDE which is suitable to study cosmic-ray physics.

ALICE is composed of several detector systems, however for the analysis presented in this thesis, which involves only one vector meson produced at mid-rapidity only some systems are needed: Inner Trackig System (ITS), Time Projection Chamber (TPC), Time of Flight (TOF); all located in the central barrel and V0, ZDC and Diffractive detector (AD); situated at forward rapidities, see Figure 4.6. These detectors will be discussed in the following. A detailed overview of ALICE and of its performance is given in [58] and [59], respectively.

4.4.1 Inner Tracking System

The Inner Tracking System (ITS) is the closest sub-detector to the beam pipe, placed the nearest to where a collision occur. It consists of six cylindrical concentric layers with radii between $3.9 < r < 43$ cm, each two layers with different technology, see Figure 4.7. The ITS covers the $|\eta| \leq 0.9$ pseudorapidity range. As it is the closest detector to the beam pipe, ITS is able to determine the primary vertex and also secondary vertices caused by decaying short-lived particles, thus the amount of the material used is required to be kept at minimum. It was designed to cope with a high particle multiplicity environment of up to

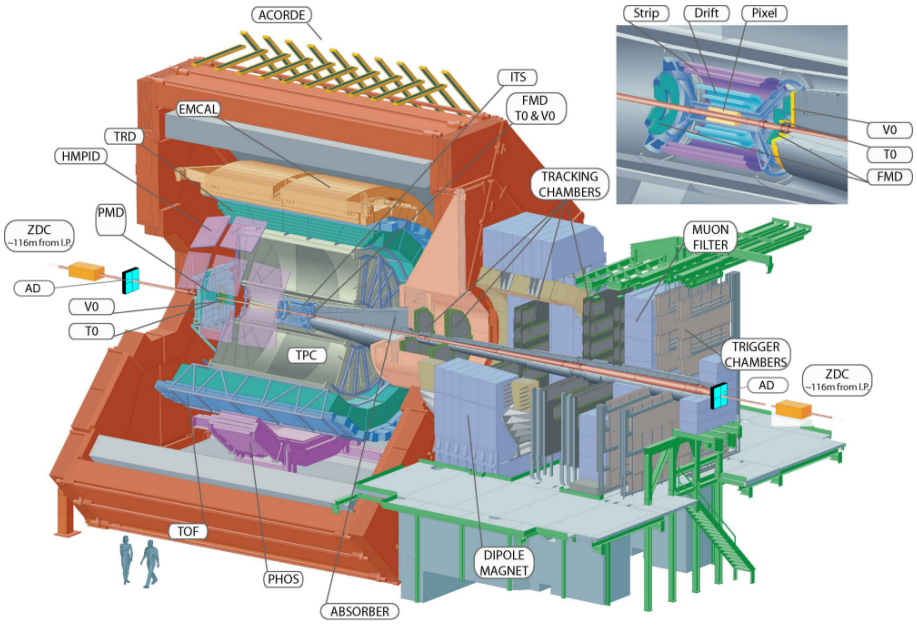

Figure 4.6: Status of the detector in 2012, taken from [60], with the AD detector modules superimposed in blue.

8000 particles per unit rapidity as it was estimated for Pb-Pb collisions [61, 62]. Because of this large number of particles a high-granularity was needed to keep the system occupancy on the order of few percent. The inner part of the ITS, the Silicon Pixel Detector (SPD) also serves for triggering. In addition, the ITS is used to determine the energy loss of particles and it can also act as an stand-alone trackers [63].

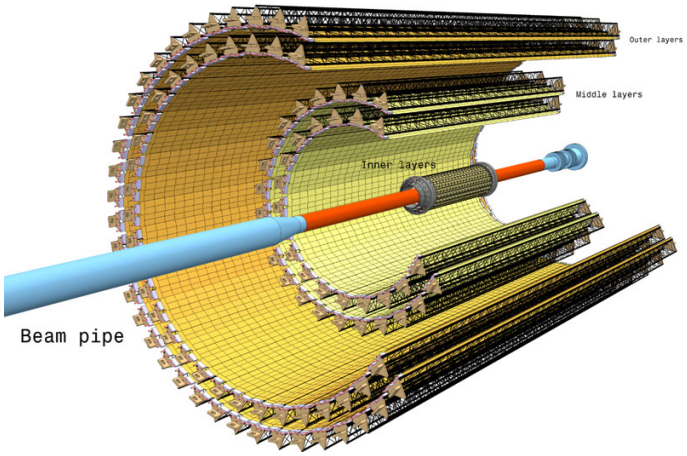

Figure 4.7: Sketch of ITS detector with its 6 layers [64].

4.4.2 Silicon Pixel Detector

The two innermost layers form the Silicon Pixel Detector (SPD), which is located at a radial distance of 9 mm from the beam tube. Its acceptance is large $|\eta| < 1.95$. As it is close to the point where the incoming beams collide, it must be able to detect primary vertices which requires high precision and granularity with the resolution of the order of 100 μm and also must withstand high-radiation. In this zone, more than 50 tracks per cm^2 are produced, thus it requires sophisticated construction.

The SPD consists of two modules mounted together. Each module forms a 141.6 mm long half-stave in the z-direction. Two head-to-head half-staves are attached to a carbon-fibre support sector along the z-direction. The carbon-fibre support sector also provides cooling. Each of these sectors contains 6 staves which are located as follows: 2 on the inner part and 4 on the outer part, see Figure 4.8 right. Each stave is assembled in the such a way that they overlap. When 5 sectors are mounted together they create a half barrel, which when it is united with another half barrel around the beam pipe, it forms a full barrel. To sum up there is in total 10 sectors supporting 60 staves, consisting of 240 modules and each stave has 20 read-out chips. Thus there are 1200 chips for a total 9.8×10^6 read-out channels [63].

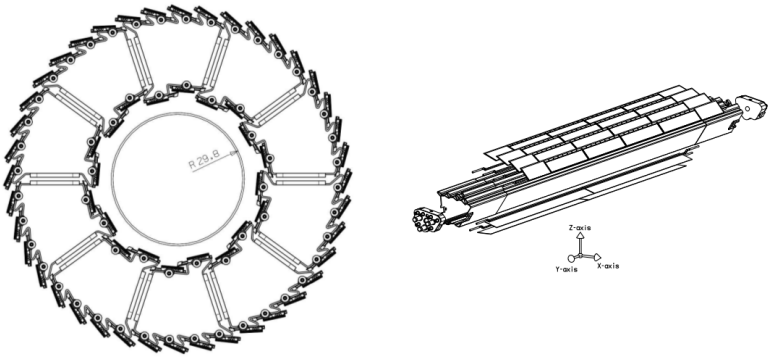

Figure 4.8: Left: Transverse cut of the SPD detector with 10 sectors carrying staves. Right: The carbon-fibre support sector with 6 staves. Taken from [65].

4.4.3 Silicon Drift Detector

The two middle layers of the ITS located between 15 cm to 23.9 cm, are called the Silicon Drift Detector (SDD) which covers the pseudorapidity region of $|\eta| < 0.9$, see Figure 4.9. Its function is to identify particles by their energy loss.

The SDD is composed of two drift regions in which electrons are moving in opposite direction in a drift field of ≈ 500 V/cm^2. There are 291 cathode strips in each drift region on both sides of the detector and also each drift region contains 256 collection anodes. The total number of cells is 89.1×10^3 and they are read out by 512 readout channels [65]. The modules of the SDD are mounted on linear structures called ladders, see Figure 4.10. 14 ladders with 6 modules each are located on the inner part of a SDD layer, while 22 ladders with 8 modules each are on the outer SDD layer [65]. Like in the SPD there are staves overlapping, thus in the SDD the modules and ladders are assembled in a way they overlap each other to cover a sensitive area larger than 580 μm and to provide full angular coverage.

Ladders are space frames made of Carbon-Fire Reinforced Plastic (SFRP) containing a protecting film against humidity absorption.

As the drift speed depends on the temperature, it is required to control and to calibrate the temperature during the data taking.

4.4.4 Silicon Strip Detector

The fifth and sixth layers forms the Silicon Strip Detector (SSD) and are located at radii of 38 cm and 43 cm respectively covering $|\eta| < 0.97$. The function of the SSD is to perform

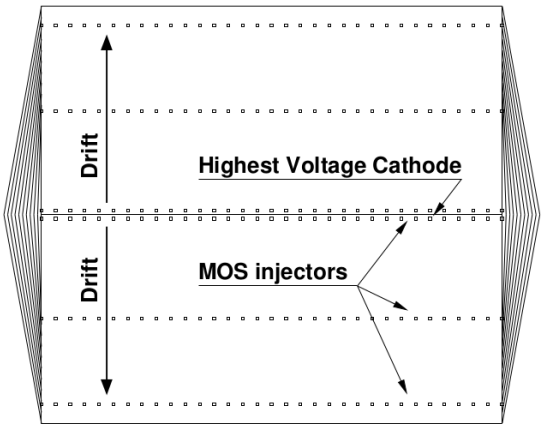

Figure 4.9: The transverse cut of the SDD module where cathodes can be seen. Taken from [65].

two-dimensional measurements of the track position as well as energy loss measurements for particle identification at low p_T.

The basic building block of the SSD detector is a module composed of one double-sided strip. The sensors are 300 μm thick and each sensor on each side has 768 strips which are almost parallel to the beam axis. The reason why they are located in this way is to provide the best resolution in z direction which is 830 μm. The mentioned modules are assembled in ladders as it was in the case of SDD, see Figure 4.10. The fifth layer of ITS, the innermost layer of SSD, contains 34 ladders and each of them has 22 modules, while the outer layer contains 38 ladders with 25 modules each. It is designed to overlap in active areas, thus it provides full coverage.

In total, there are 72 ladders with 1698 modules mounted on Carbon Fibre Composite support cones in two cylinders. The carbon fibre has very good properties. It is lightweight, so it minimizes the interaction with newly created particles and at the same time it is a stiff material, so it would not bend. The ladders are 120 cm long, the sensitive area of the fifth layer of the ITS is 88 cm and of the sixth layer accounts for 100 cm.

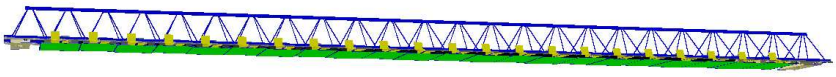

Figure 4.10: The SDD and SSD ladder. Taken from [65].

4.4.5 Time Projection Chamber

The Time Projection Chamber (TPC) is one of the most sophisticated ionization detectors. The TPC is 3-dimensional tracking detector providing information of many points on a particle track and of the specific energy loss of the particle. It is also called *electronic bubble chamber*. It is a cylindrical detector filled with gas composed of 90 % of $C_2H_2F_4$, 5% of i-C_4H_{10} and finally of 5% of SF_6 enclosed in a volume of 90 cm^3. Its inner radius is 80 cm, outer radius has 250 cm and the length along the z-axis is 500 cm. The TPC covers a pseudorapidity region of $|\eta| < 0.9$ and it is constructed from a low budget material to avoid as much as possible multiple scattering and secondary production of particles [66].

The particle tracking in the TPC can be done in a wide momentum range $0.1 \leq p_T \leq 100$ GeV/c with a good momentum resolution. The limiting factor is the previous interaction of the particles with the material of the ITS.

At the centre of the TPC it is situated a high voltage electrode, see Figure 4.11, which creates en electric field along the axis of the beam. A magnetic field parallel to the electric field is also present. The cylindrical detector ends by endcap wire chambers consisting of cathode pads. When a particle passes through the TPC it produces free electrons, which drift towards the endcaps and subsequently are detected by the anodes. Every drifted electron will end in the endcap leaving a sample of the track. This implies a lot of space points allowing a full reconstruction of the particle trajectory.

The problem is the long drift distance. Diffusion is caused particularly in the lateral parts of the TPC. The solution to this problem is a parallel magnetic field. It confines the electrons trajectories and thus reduces the diffusion by a factor of 10. In addition, the magnetic and the electric field must be in perfect alignment to avoid deviating the trajectories of the drifting electrons.

Another problem occurs with the positive ions which are accumulated when the electrons are drifted to the anodes. These positive ions could return towards the sensitive area since there it is located the cathode. This phenomenon causes a distortion of the electric field. To prevent this effect a grid is placed at the ground potential before the anode wires. The positive ions do not return to the sensitive area and they are rather captured at this grid.

As it was mentioned already, the TPC detector is suitable to determine the type of particle based on the energy loss of this particle, see Figure 4.12. This can be done since the charge collected at the endcap is proportional to the energy loss of the particle and thus the signal amplitudes from the anode provide information on the energy loss of the particle.

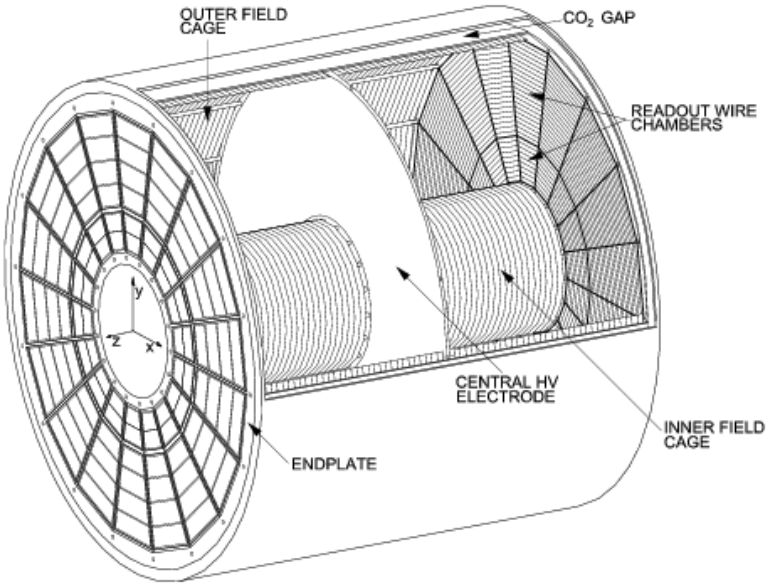

Figure 4.11: The schematic figure of the TPC. Taken from [67].

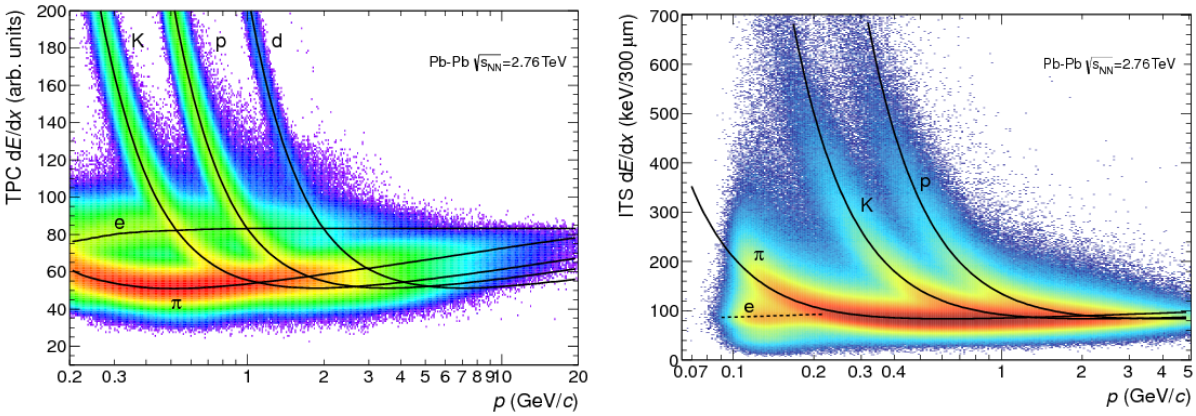

Figure 4.12: Comparison of the energy loss dE/dx of determined particles in TPC at ALICE (left) with the energy loss in ITS at ALICE (right) [59].

4.4.6 Time of Flight

The main goal of the Time of Flight (TOF) detector is the identification of charged particles at pseudorapidities covering $|\eta| \leq 0.9$ although for our analysis the main use is triggering. TOF is 741 cm long, the internal radius is 370 cm and the external is 399 cm, see Figure 4.14.

Particle identification is provided combining the time-of-flight of the particle with information on the momentum and track length given by the TPC. To identify and separate pions and kaons up to transverse momenta of 2.5 GeV/c and protons up to 4 GeV/c, the total time resolution is needed to be < 100 ps. The TOF is composed of an array of double-stack Multiple-gap Resistive Plate Chamber (MRPC), which covers the full azimuthal angle.

The detector is divided in 18 segments, each has 7.5 m in length and these segments are also called supermodules (SM) or azimuthal sectors. Each of the segments contains five gas-tight modules located along the beam-axis. External and intermediate modules contain 19 MRPC and the central one contains 15 MRPC, which also can be denominated as *strips*. These strips are inclined in different angles to avoid dead zones.

Supermodules possess, in addition to the MRPC, the cooling and gas distribution system and the front-end readout board. In total, TOF contains 96 readout pads with 152928 readout channels and covers an area of 141 m^2 resulting in low occupancy and good performance [66].

4.4.7 V0

The V0 detector was designed for triggering and to separate beam-beam interactions from the accelerator background, the so-called *beam-gas*. Another task of V0 detector is to estimate the centrality of the collisions and to measure the luminosity, which is required to determine absolute cross-sections.

The V0 detector consists of two parts; arrays of scintillator counters V0A and V0C. They are installed in opposite sides along the beam pipe, see Figure 4.15. V0A is located at a distance of 340 cm from the interaction point (IP) on the opposite side to the muon spectrometer, while V0C is located on the side of the muon detector, 90 cm from the IP. V0A covers pseudorapidities $2.8 < \eta < 5.1$ and V0C covers $-3.7 < \eta < -1.7$. They are perpendicular to the beam line [70].

These arrays are segmented into 4 rings and each ring is divided in 8 azimuthal cells.

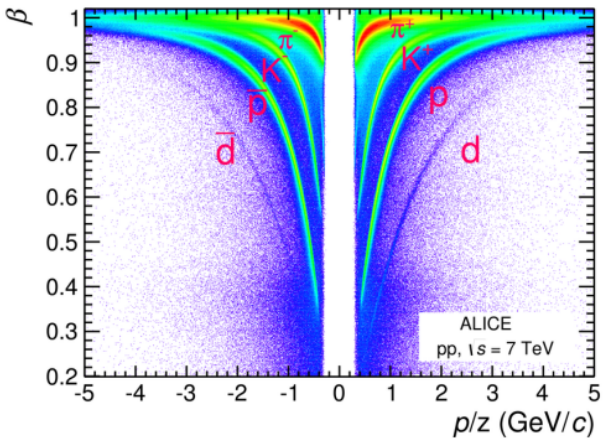

Figure 4.13: The measurement of particle identification provided by TOF at ALICE [68].

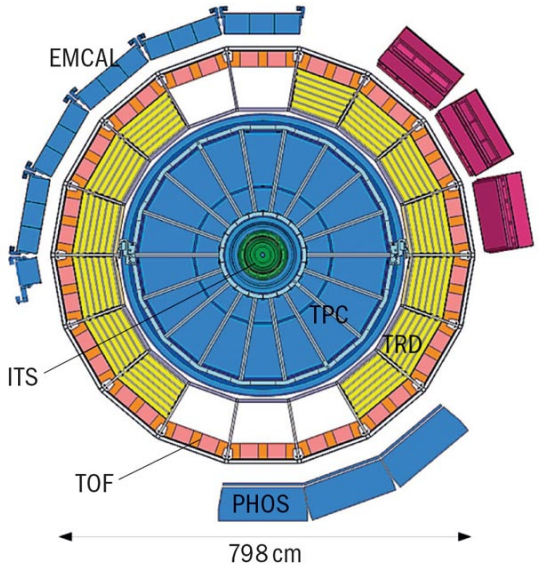

Figure 4.14: Transverse cut of the ALICE detector, where ITS, TPC and TOF are depicted [69].

In total there are thus 32 cells in each array. Each cell is connected to PMTs with 1 mm diameter Wave-Length-Shifting fibres (WLS), see Figure 4.16.

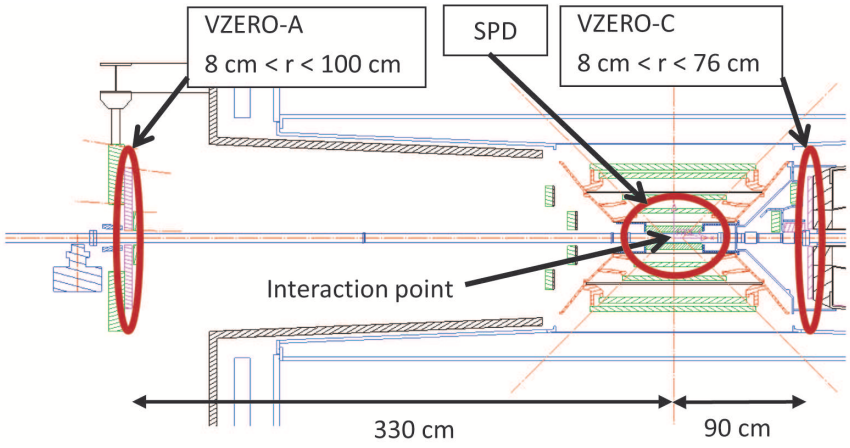

Figure 4.15: The position of V0s detectors on a sketch of the part of ALICE detector [71].

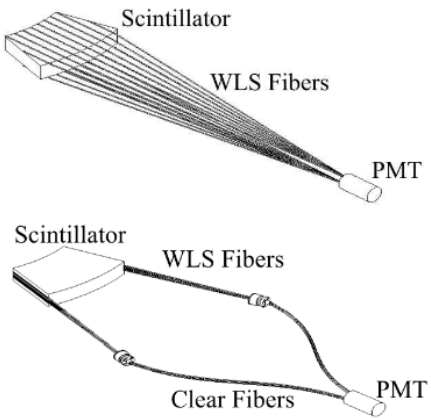

Figure 4.16: At the top is the schematic sketch of a V0A cell and at the bottom is a cell for the V0C with WLS fibres [72].

4.4.8 Zero-Degree Calorimeter

The main function of the quartz spaghetti fibre calorimeter called Zero-Degree Calorimeter (ZDC) is to determine the centrality of the collision taking advantage of the fact that spectator nucleons keep the direction along the beam pipe and hit the ZDC, see Figure 4.17. For this reason ZDC are located at a distance of 112.5 m on either side of IP, at zero degrees.

Since the ZDC has very good time resolution it is also used to reject out-of-time background created when particles of one beam fall in the wrong radio frequency bucket and collide with the second beam [66].

Each ZDC is composed of two calorimeters: neutron calorimeter (ZN) and proton calorimeter (ZP). The spectator neutrons are measured with the ZN which is located between the beam pipes, while the proton spectator, ZP, is placed at the external part of

the outgoing beam pipe. At this place the positive particles are deflected by the magnetic field and thus are separated from the neutrons.

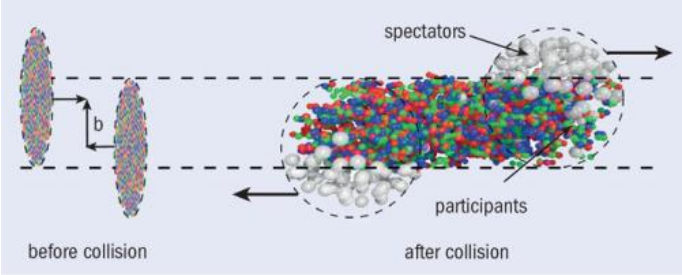

Figure 4.17: Diagram of the process of a collision [73].

Other two calorimeters are electromagnetic calorimeters denominated as ZEM. They are situated at a distance of 7 m from IP in the side where there is no muon spectrometer and also are located on both sides of the beam line. The main task of ZEM is to distinguish central, peripheral and ultra-peripheral collisions.

4.4.9 The Diffractive detector

The diffractive detector (AD) was installed during the long shutdown period between Run1 (2009-2013) and Run2 (started in 2015), so it is available only for analyses with Run2 data. AD consists of 2 groups of 4 scintillator stations, each consisting of two scintillating pads, situated at forward pseudorapidities. One group of stations of AD are situated on the A side ($z > 0$); The first layer at $z = 1695.17$ cm and second layer at $z = 1698.17$ cm from the interaction point (IP) and the rest of stations are on the C side ($z < 0$) located at $z = -1952.9$ cm and $z = -1955.9$ cm. The AD detector covers a wide pseudorapidity range: $4.9 < \eta < 6.3$ and $-6.9 < \eta < -4.9$ for the A and C sides, respectively. This pseudorapidity coverage improves the acceptance for diffractive systems with masses below 10 GeV/c^2.

Charged particles generate light passing through the scintillator layers. This light is collected by wave-length shifting (WLS) bars, see Figure 4.18. WLS are connected to photomultiplier tubes by optical fibres.

4.5 The ALICE trigger system

Depending on the LHC running conditions, there may be collisions as frequently as each 25 ns. However not all events are suitable to study a particular branch of physics. Those events which are of interest must be selected according to special requirements. This process is complex and is provided by the trigger system. The process of collecting and processing the events can be divided in two parts: online control system and offline framework.

4.5.1 Online control system of ALICE

The online control system of ALICE consists of several parts, namely: Detector Control System (DCS), Central Trigger Processor (CTP), The Data Acquisition (DAQ), High Level Trigger (HLT), Data Quality Monitoring (DQM), Detector Algorithms (DA) and Trigger System (TS).

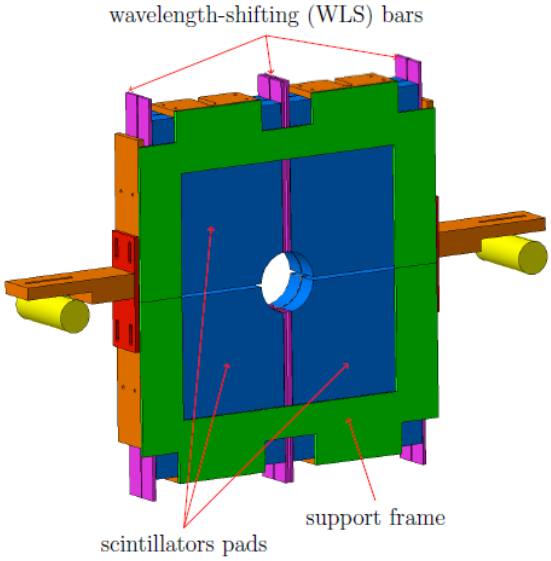

Figure 4.18: The scheme of the layer of AD detector with WLS , hole for the beam pipe, scintillators pads and the support frame. Taken from AD note which is work in progress.

4.5.2 Detector Control System

The name Detector Control System indicates that its main function is to control detectors during data taking. It allows to check possibles errors in the different subsystems and issues instructions to recover from these failures, thus maximizes the efficiency of the data acquisition.

4.5.3 Central Trigger Processor

Each triggering detector, which is a sub-detector generating a trigger decision, sends signals (also called inputs) to the Central Trigger Processor (CTP). The CTP then ships raw data to the Data Acquisition System via Detector Data Links (DDL). Besides this process, the data are copied to the High Level Trigger (HLT) for online processing, which will be discussed below.

The time between the moment when a collision occurs till the moment when a signal from the interaction is sent to the trigger system is called latency. Every trigger signal has a different latency. According to this fact, the inputs with similar latencies together form different levels. The function of the levels is to reject unsatisfying events as soon as possible and thus reduce the dead time of the system.

The maximum number of the trigger inputs is 60, divided in three levels as following: 24 for Level 0 (L0), 24 for Level 1 (L1) and 12 for Level 2 (L2), [74].

The L0 has a short latency, the trigger decision must be made in less than 1.2 μs thus the L0 inputs arrive at the detector within 800 ns. that means that the L0 is the fastest trigger signal. For the type of physics studied in this thesis, see Chapter 5, the L0 inputs come from SPD, V0, TOF and muon trigger.

Another fast trigger signal is L1 which arrives at the detector in 6.1 μs after the collision which allows to make a decision in 6.5 μs. The L1 inputs are from ZDC and other sub-detectors. Both L0 and L1 carry out the first physics selections.

It is necessary to take into account pile-up effects which may contaminate the data

sample. To see if the signal was produced because of pile-up and to search for requested events in a time window before and after the collision is responsibility of the past-future protection circuit (p/f) [75].

Although every level checks p/f, the slowest level which waits for p/f is L2. Because of the long drift time the inputs from L2 arrive at the CTP 88.7 μs after the interaction, which gives the necessary time to the CTP to decide about the selection. In this case the decision time is 88 μs.

4.5.4 Data Acquisition

The main function of DAQ is to move the data from the sub-detectors to the central data storage of ALICE. It handles a large amount of the data, about 1.25 GB/s. When the CTP decides to take the event, a signal is sent to the front-end read-out electronics (FERO) in the particular detector. Then the data are injected into DDLs and sent out to the farm of computers called Local Data Concentrators (LDC). These LDCs are responsible for building the fragments of events from FERO to sub-events. These are then shipped to the Global Data Collectors (GDC) where every sub-event is taken from all LDCs and thus is built a whole event which is then sent to the storage facilities [75], see Figure 4.19.

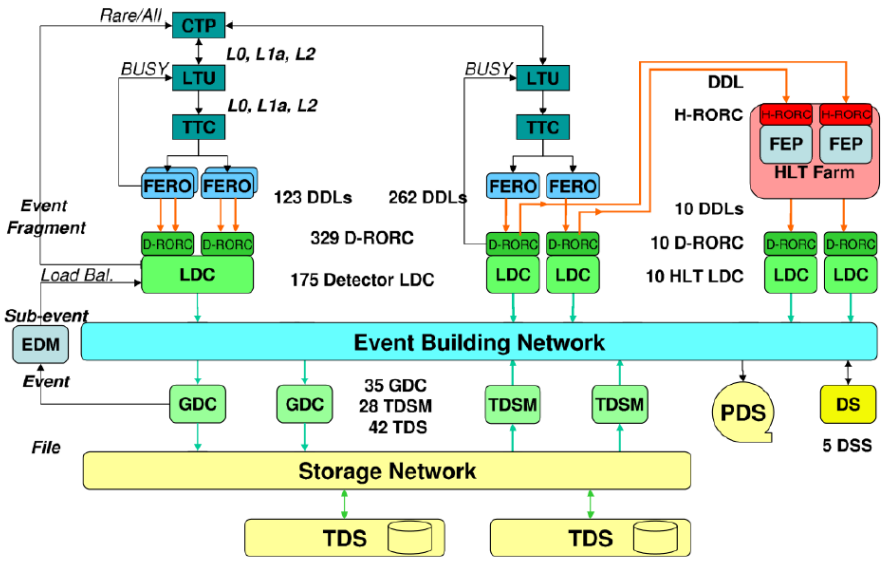

Figure 4.19: The scheme of DAQ. Taken from [58].

4.5.5 High Level Trigger

The HLT builds up the global event by selecting interesting data and thus reduces the data size. It consists of a farm of more than 1000 multi-processor computers and shows the online event display which allows to control the quality of the data taking.

4.5.6 Data Quality Monitoring

From the name it is clear that this part of the online control trigger system is responsible to assess the quality of the acquired data based on online feedback. As it provides online feedback it allows the visualization and monitoring of samples, thus gives the possibility to discover fast potential problems and to correct them

4.5.7 Detector Algorithms

DA allows to calibrate readout electronics and thus to reduce the systematic uncertainties. Each DA produces online results which can be directly used or stored offline to be used for the reconstruction.

4.5.8 Offline Framework - Aliroot

The offline framework for the ALICE collaboration is called Aliroot and has a lot of functions as following: simulation, reconstruction, detector alignment, calibration, visualization and analysis of data [75]. The main language is C++ and it is based on the ROOT system. Aliroot is designed to interface easily with Monte Carlo (MC) generators.

4.6 The GRID and LEGO trains

From the description above it is obvious that the large amount of real data must be stored somewhere, in addition these real data also have to be replicated more times. It is required to have a computing infrastructure which is called The Grid.

The GRID is an infrastructure which has a hierarchical order called Tiers which are located all over the world, see Figure 4.20. The real data are stored at CERN, which is called Tier-0. Data are stored in three formats: RAW, as it comes from the subdetectors, ESD (event summary data), which contains a mixture of detector level information and physics quantities, and AOD (analysis object data) which has information at the level of objects used directly for analyses.

Then the data are replicated in regional large computing centres at Tier-1. Smaller local resources like institutes are part of Tier-2. Below this Tiers are Tier-3 and Tier-4 which are even smaller local resources formed by university departments and user's workstations. All Tiers are connected via GRID Midleware and particularly for ALICE the Midleware services are called AliEn through which the user can communicate with the GRID [75]. To analyse the data over the GRID in an efficient way, ALICE has a system called LEGO Analysis Trains, which are composed of so-called wagons, each of which performs an specific analysis. All wagons in the train access the same data, so that data has to be read only once.

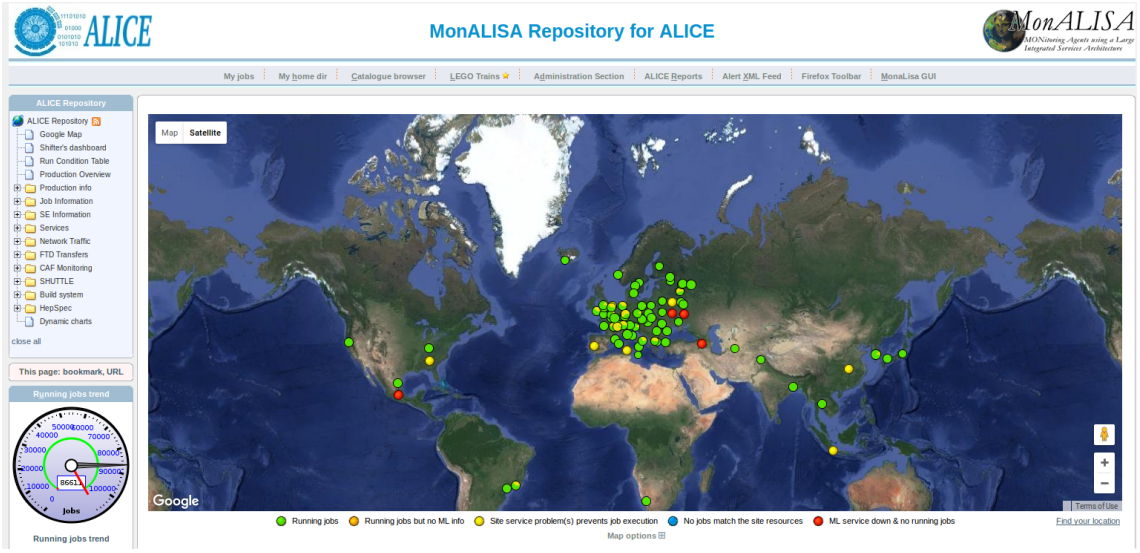

Figure 4.20: The GRID infrastructure. Taken from [76].

ALICE is divided in so-called physics-working groups. Each group has their own set of trains. The analysis that is presented in this thesis, was carried out within the PWG-UD, specifically within the PAG-UPC, where PAG is an acronym for physics-analysis group.

The data used as input to the analysis to be presented in Chapter 7 is the output of one of the LEGO Trains of the PWG-UD group.

Chapter 5

Ultra-peripheral collisions

After having introduced in Chapter 3 the physics we are interested in, namely the behaviour of the gluon distribution of hadrons at small x, and in Chapter 4 the infrastructure we use, LHC and ALICE, in this chapter we present the type of events we want to measure and how they relate to the gluon distribution at small x.

When two heavy nuclei, for example Pb, interact at large impact parameter b with respect to the sum of their radii $R_{1,2}$, see Figure 5.1, the only way available for these nuclei to interact is by the electromagnetic field. For the case of fast ions, this field can be expressed by its Fourier transform, which in this case, has the mathematical form of a flux of photons. Because of the condition of a large impact parameter, they are called ultra-peripheral collisions (UPC). Since there is a large impact parameter, the dominant interaction in UPC is the electromagnetic interaction while the hadronic interaction is strongly suppressed.

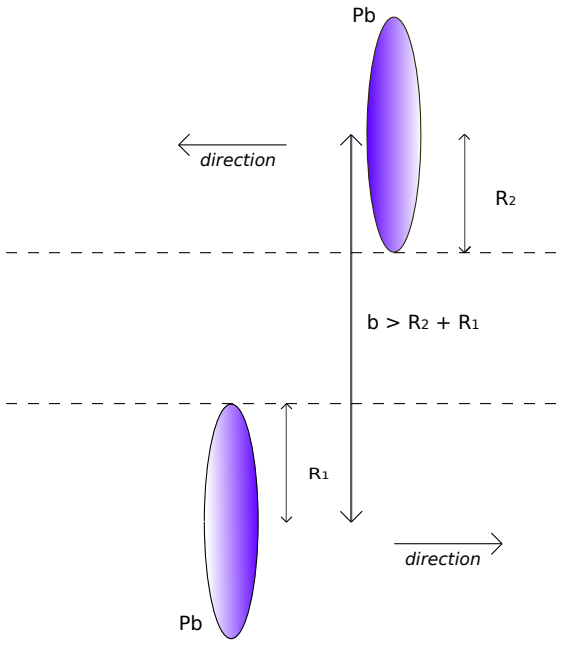

Figure 5.1: Diagram of an ultra-peripheral collision. The gradient of the colour represents the direction of movement of the Pb.

The intensity of the photon flux is proportional then to Z^2 with Z the electric charge of the ion. The maximum energy reached by the flux is limited by the boost of the source in the laboratory frame, which is several TeV at the LHC.

The interaction may occur in different ways. The photon from the projectile (ion of Pb) can interact with the photon emitted from the target (another ion of Pb). Or on the other hand, the photon emitted from projectile (ion of Pb) can interact directly with the target (another ion of Pb), see general example in Figure 5.2 a) and b) respectively.

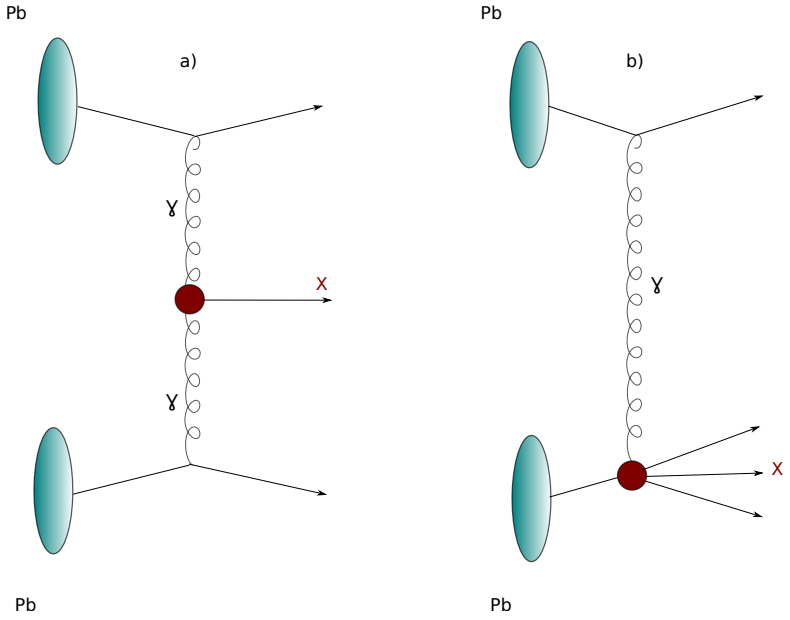

Figure 5.2: The illustration of the manner how the nuclei interact via the photons.

We are interested in this second class of events, where the system X in Figure 5.2 (b) is composed of a vector meson and a lead ion, with no colour flow between them, as illustrated in Figure 5.3. The photon interacting with the target fluctuates into a quark-antiquark pair which then interacts with the target. For the case when there is a charm-anticharm pair, one can apply perturbative QCD, and attempt to compute this process as the interaction of this colour dipole with the target through the interchange of a colourless configuration of gluons. To describe this phenomena a convenient reference frame is any in which the quark-antiquark pair lives a long time to be able to interact with the target. As a consequence of the interaction a vector meson with small transverse momentum is created.

In this thesis, we are interested in the coherent photoproduction of the $\psi(2S)$ vector meson. Here the word coherent, means that the dipole interacts with the full colour field of the target coherently to create the vector meson of the $\psi(2S)$, which means that in the final state there is only the vector meson (VM) produced with relatively small p_T, see Figure 5.4. The property of the small p_T is a characteristic for coherent photoproduction, $p_T \approx 60$ MeV/c.

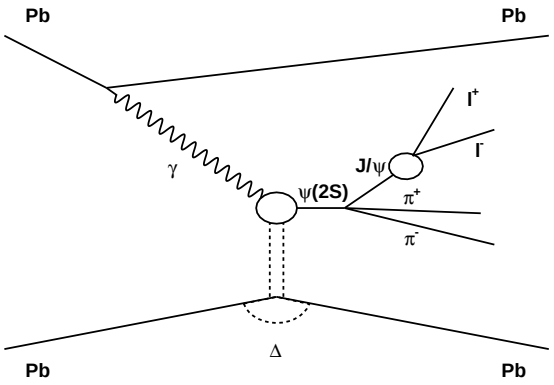

Figure 5.3: Diagram for the coherent photoproduction off lead nuclei of a ψ(2S) vector and its subsequent decay into a J/ψ and two pions.

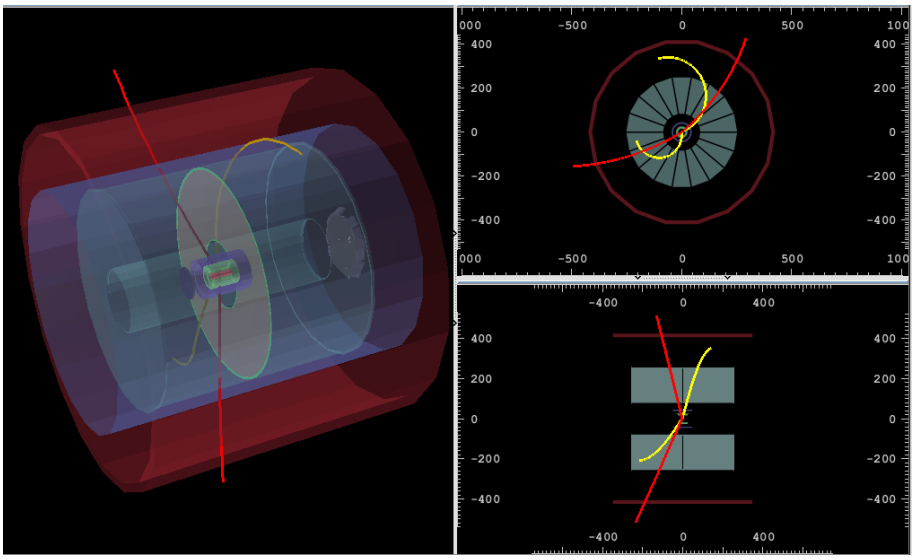

Figure 5.4: An event for coherent photoproduction of the ψ(2S) from PbPb collision in ALICE at $\sqrt{s_{NN}} = 2.76$ TeV from Run1. The red lines correspond to the $\mu^{\pm}$ and the yellow lines to the $\pi^{\pm}$.

5.1 Experimental observables of ψ(2S)

Experimental observables of the ψ(2S) are its p_T and its rapidity. The rapidity of ψ(2S) is given by the following formula

$$y = \ln\frac{(p_0 + p_z)}{(p_0 - p_z)}, \tag{5.1}$$

where p_0 and p_z refer to the zero and third entries of the four momenta of the vector meson, respectively. Once we have defined the rapidity of ψ(2S), we can write down the equation relating the rapidity with the centre-of-mass energy of the photon-target $W_{\gamma Pb}$ system, given by:

$$(W_{\gamma Pb})^2_{\pm} = 2\omega_{\pm}\sqrt{s}, \tag{5.2}$$

where $\omega_{\pm}$ is the energy of the photon, given by

$$\omega_{\pm} = \frac{\mathrm{M}}{2}\exp(\pm|y|) \tag{5.3}$$

M is the mass of the vector meson and $\sqrt{s}$ is the centre of mass energy of the Pb-Pb.

The cross section for the coherent photoproduction of a vector meson in a Pb-Pb UPC is given is given by the following equation:

$$\frac{d\sigma_{PbPb}(y)}{dy} = N_{\gamma/Pb}(y, M)\sigma_{\gamma/Pb}(y) + N_{\gamma/Pb}(-y, M)\sigma_{\gamma/Pb}(-y), \tag{5.4}$$

where M is the mass of the ψ(2S), y is the rapidity in the laboratory system

$$y = \ln\left(\frac{2\omega}{M}\right), \tag{5.5}$$

ω is the energy of photon, the $\sigma_{\gamma/Pb}(y)$ is the cross-section of the corresponding photoproduction and $N_{\gamma/Pb}$ is the photon flux. Since we have two symmetric relativistic heavy ions the probability of emitting the photon at mid-rapidity (y=0) is the same for both nuclei, see Eq. (5.4).

In perturbative QCD, assuming one value of x is enough to describe the interaction, one can write

$$x = \frac{M^2}{W^2}. \tag{5.6}$$

With higher energy, we can reach the smaller x. This means, that the measurement of the vector meson at different rapidities samples different values of x. Using Equations (5.2) and (5.3), and taking into account that we are interested in the measurement at $y = 0$, for collisions at $\sqrt{s} = 5.02$ TeV, we obtain $W_{\gamma Pb} = 272$ GeV, which implies, using Equation (5.6) $x = 1.8 \times 10^{-4}$. So indeed, this process access the gluon distribution of lead nuclei at very small values of x.

In summary, coherent photoproduction of vector meson in Pb-Pb UPC, is sensitive to the gluon distribution of the target at small x. Furthermore, these events have a striking signature: only the tracks from the decay products of a vector meson are present in the event[1], and the transverse momentum of the vector meson is expected to be very small, of the order of 100 MeV.

[1]Due to the intense electromagnetic fields of the incoming ions, there may be extra independent interactions between them. These interactions may excite one or both of the nuclei, which upon de-excitation may emit one or a few neutrons in the forward direction.

Because the p_T is so small, in two body decays, the decay particles are produced back-to-back in azimuth. In the four body decay, the J/ψ has also very small p_T, so that also in this case the decay particles are produced back-to-back, see Figure 5.4. This property is used in the trigger.

Chapter 6

Previous measurements of charmonia in Pb-Pb UPC

UPC are not only studied in ALICE at CERN but also in other experiments. The first measurement of the UPC photoproduction with heavy-ion was performed by PHENIX at RHIC in BNL in 2009. Later ALICE has reported the measurement of both J/ψ and ψ(2S) coherent photoproduction and recently CMS has also measured J/ψ coherent production.

6.1 PHENIX measurement

This experiment measured ultra-peripheral collisions of Au+Au producing exclusively e^+e^- pairs at mid-rapidity at an energy of $\sqrt{s_{NN}}$ = 200 GeV at RHIC in BNL. The data were collected during the 2004 high-luminosity Au+Au run. The total number of events which passed the UPC trigger was 8.5 M. From these events 6.7 M were suitable for further analysis and corresponded to an integrated luminosity of $\mathcal{L}_{int} = 141 \pm 12\ \mu\text{b}^{-1}$ [77].

The cross section of J/ψ production in UPC at mid-rapidity can be seen in Figure 6.1 where it is compared to theoretical calculations. The statistical uncertainties are shown as the error box. Since the statistical errors are quite large, the measurement do not allow to put constrain in any of the theories. But this measurement was a clear sign that UPC can be measured in heavy ion collisions.

6.2 Coherent and incoherent measurement of J/ψ at ALICE

Another measurement for photoproduction in UPC for coherent and incoherent J/ψ production in collision of Pb-Pb heavy ions was done at ALICE, in the rapidity region $-0.9 < y < 0.9$ with integrated luminosity of $\mathcal{L}_{int} = 23.0^{+0.7}_{-1.2}\ \mu\text{b}^{-1}$ [78]. These studies included and extended the first measurement of coherent production of J/ψ ever, performed by ALICE and reported in [79].

The study was done for two channels: J/$\psi \to e^+e^-$ and J/$\psi \to \mu^-\mu^+$. The coherent photoproduction yield for the first channel was $N^{coh}_{yield} = 265 \pm 40(\text{sta}) \pm 12(\text{sys})$ and for the second channel of muons was a little higher $N^{coh}_{yield} = 291 \pm 18(\text{sta}) \pm 4(\text{sys})$. The cross section was calculated from the following equation:

$$\frac{\mathrm{d}\sigma^{\mathrm{coh}}_{\mathrm{J}/\psi}}{\mathrm{dy}} = \frac{N^{coh}_{\mathrm{J}/\psi}}{(\mathrm{Acc} \times \epsilon)_{\mathrm{J}/\psi}\mathrm{BR}(\mathrm{J}/\psi \to \mathrm{l}^+\mathrm{l}^-)\mathcal{L}_{\mathrm{int}}\Delta\mathrm{y}}, \tag{6.1}$$

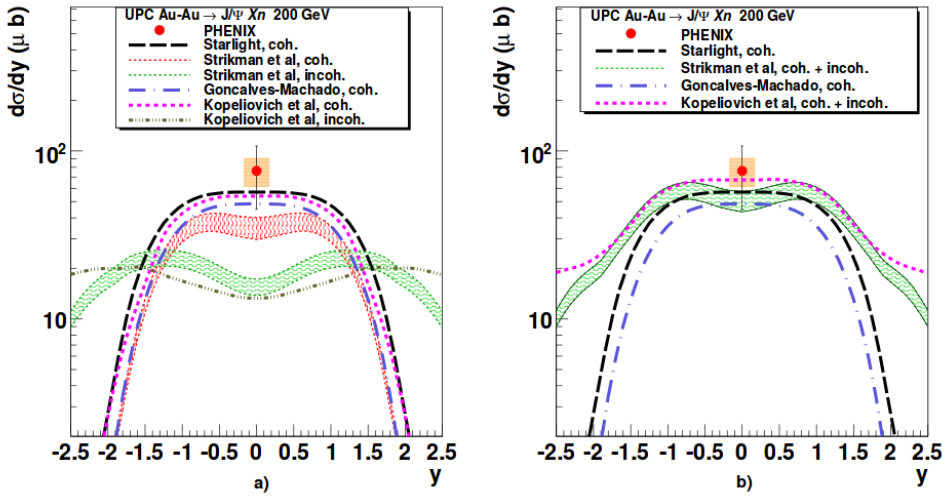

Figure 6.1: The cross section of J/ψ production in Au-Au UPC at PHENIX. Taken from [77].

where $N^{coh}_{\mathrm{J}/\psi}$ is the number of the coherent events, the $(\mathrm{Acc}\times\epsilon)_{\mathrm{J}/\psi}$ is the corresponding acceptance and efficiency, the $BR(\mathrm{J}/\psi \to l^+l^-)$ is the branching ratio, Δy is the width of the rapidity range and $\mathcal{L}_{int}$ is the integrated luminostiy [78].

The combined weighted average cross section of the di-electron and the di-muon channel is then $\mathrm{d}\sigma^{coh}_{\psi(2\mathrm{S})}/\mathrm{d}y = 2.38^{+0.34}_{-0.24}$ (stat + sys) mb.

The same system was used to calculate the cross section for the incoherent samples although the yield was quite different $N^{coh}_{yield} = 61 \pm 14(\mathrm{sta})^{+16}_{-7}(\mathrm{sys})$ for the decay channel of J/ψ to e^+e^-. The yield for the J/$\psi \to \mu^+\mu^-$ channel was $N_{yield} = 91 \pm 15(\mathrm{sta})^{+7}_{-5}(\mathrm{sys})$ [78]. Applying the fraction of incoherent J/ψ mesons from feed-down from the ψ(2S) decay was obtained the total number of incoherent muon events was $N^{inc}_{\mathrm{J}/\psi}(\mu^+\mu^-) = 81 \pm 13(\mathrm{sta})^{+8}_{-6}(\mathrm{sys})$ and for di-electron channel it was $N^{inc}_{\mathrm{J}/\psi}(e^+e^-) = 39 \pm 9(\mathrm{sta})^{+10}_{-5}(\mathrm{sys})$. The combined weighted average of the cross sections gave $\mathrm{d}\sigma^{inc}_{\psi(2\mathrm{S})}/\mathrm{d}y = 0.98^{+0.19}_{-0.17}$ (stat + sys) mb [78].

These cross sections are shown in Figure 6.2 and Figure 6.3 where they are compared to different models. The cross section for coherent J/ψ is in good agreement with models including moderate gluon shadowing. While the coherent cross section seems to fit the theory, the incoherent photoproduction cross section is not correctly described by models.. The LM model underestimates the measurement by a factor of 2, the RSZ-LTA by a factor of 4 and on the other hand, the STARLIGHT model overestimates the cross section by a 60%.

6.3 Coherent measurement of ψ(2S) at ALICE

The coherent photoproduction cross section of ψ(2S) in UPC at an energy of $\sqrt{s_{NN}} = 2.76$ TeV in the collision of Pb-Pb was measured by ALICE. It was the first measurement ever done for coherent ψ(2S).

The cross section was calculated similarly by the formula (6.1) but instead of J/ψ the yield of coherent ψ(2S) $N^{coh}_{\psi(2\mathrm{S})} = 17.5\pm9.0$ were used, the branching ratio was $BR(\psi(2\mathrm{S}) \to l^+l^-)$, $\Delta y = 1.8$ and the total integrated luminosity was $\mathcal{L}_{int} = 22.4^{+0.9}_{-1.2}$ $\mu\mathrm{b}^{-1}$ [80]. The channels ψ(2S) to J/ψ and two pions were also studied. All channels were used to obtain

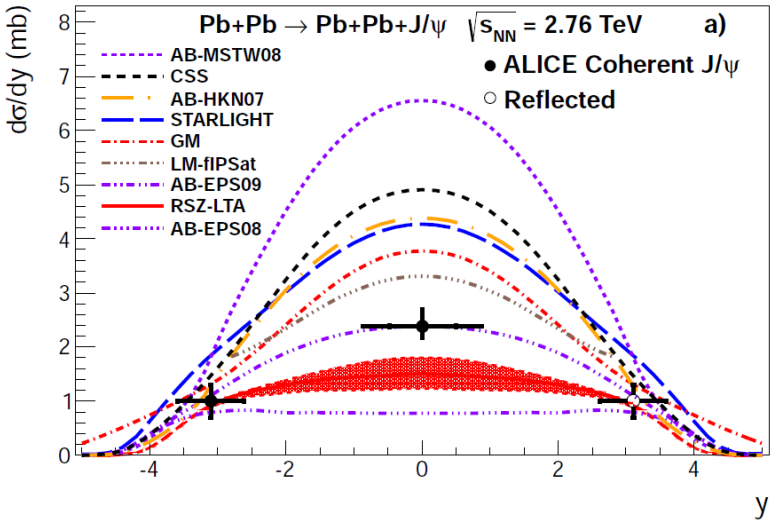

Figure 6.2: Differential cross section of coherent J/ψ production compared to different theoretical models. Taken from [78].

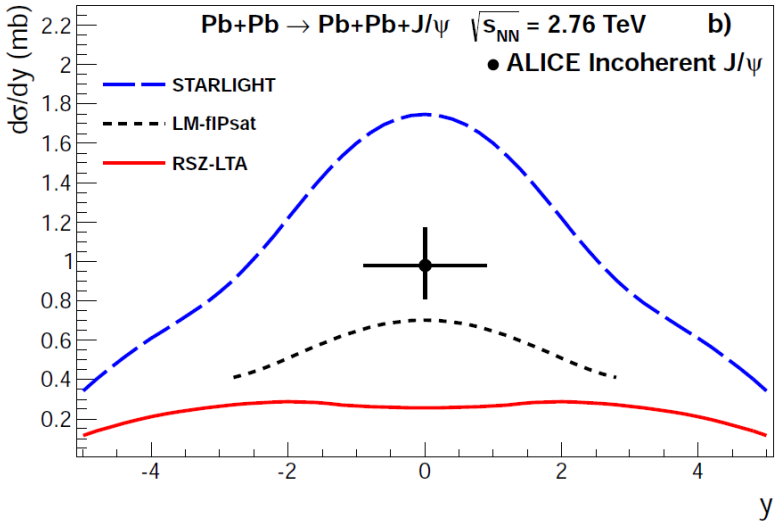

Figure 6.3: Differential cross section of incoherent J/ψ production compared to different theoretical models. Taken from [78].

the final measurement.

The measured differential cross section for ψ(2S) compared to models is shown in Figure 6.4. Models with strong gluon shadowing, the AN EPS08 and GDGM, underestimate the data by a factor of two, which means that string shadowing is disfavoured. On the other hand, models which neglect any nuclear effects fail to describe data, overestimating them by a factor of 1.5 to 3 σ [80].

It was showed that the models which include only moderate gluon shadowing like AN-EPS09 are able to reproduce the measurement although the conclusion has to be taken with care because of the statistical and systematic uncertainties, see Fig. 6.4. The ratio of the J/ψ to ψ(2S) coherent cross section is shown in Figure 6.5 compared to other measurement and model predictions. ALICE measurement is higher than data in other systems and than most model predictions. This shift of 2 σ could be caused by the statistical fluctuations but on the other hand could signify, that J/ψ and ψ(2S) production is modified by nuclear effects in a different way [80].

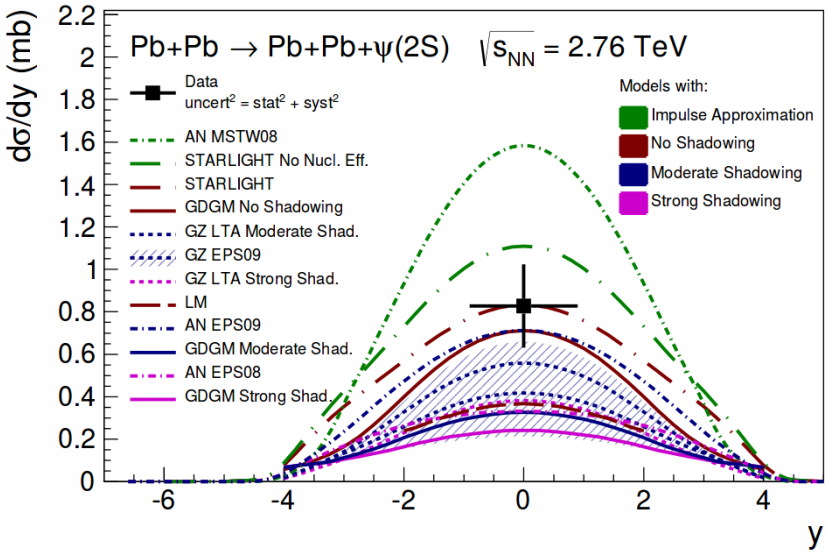

Figure 6.4: Differential cross section of ψ(2S) coherent production compared to different theoretical models. Taken from [80].

6.4 Coherent J/ψ cross section at the CMS

The coherent J/ψ photoproduction cross section in PbPb collisions in UPC was also measured by CMS at $\sqrt{s_{NN}} = 2.76$ TeV in the semi-forward rapidity region $1.8 < |\eta| < 2.3$.

Using the formula (6.1) and the coherent J/ψ yields $N^{coh}_{J/\psi} = 207 \pm 18$, integrated luminosity of $\mathcal{L}_{int} = 159\ \mu b^{-1}$, $(A \times \epsilon)^{J/\psi} = [5.9 \pm 0.5(\text{stat})]$ %, $\Delta y = 1$ and the branching ratio $BR(J/\psi \to \mu^-\mu^+) = [5.93 \pm 0.06(\text{syst})]$ % it is obtained $\frac{d\sigma^{coh}_{J/\psi}}{dy} = 0.37 \pm 0.04(\text{stat}) \pm 0.04(\text{syst})$ [81].

The data is shown in Figure 6.6, the red point is the data from CMS, which is again compared to models and to the ALICE measurement which is represented by the black square. The CMS point had to be scaled up by a factor of 5.1±0.5 to take into account that the trigger required at least one forward neutron. The models which include strong gluon shadowing like AB-EPS08 underestimate the data while the models which are based on

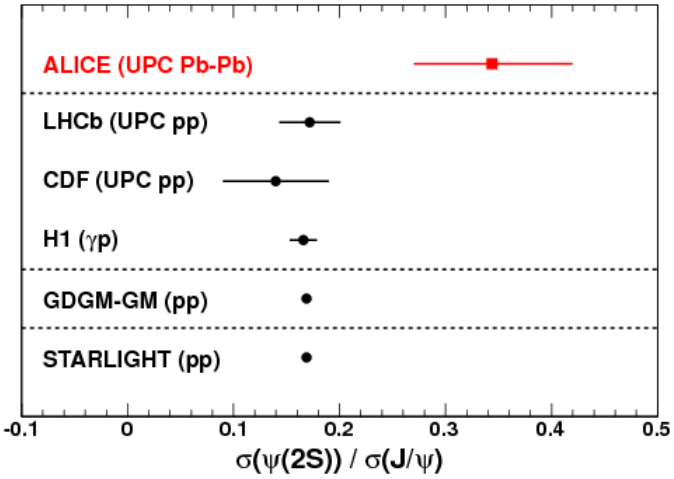

Figure 6.5: The ratio of the coherent production cross section of J/ψ to ψ(2S). Taken from [80].

moderate gluon shadowing like AB-EPS09 and GSZ-LTA [1] describe well the data. Other models which does not include any nuclear effects overestimate the measurement [81].

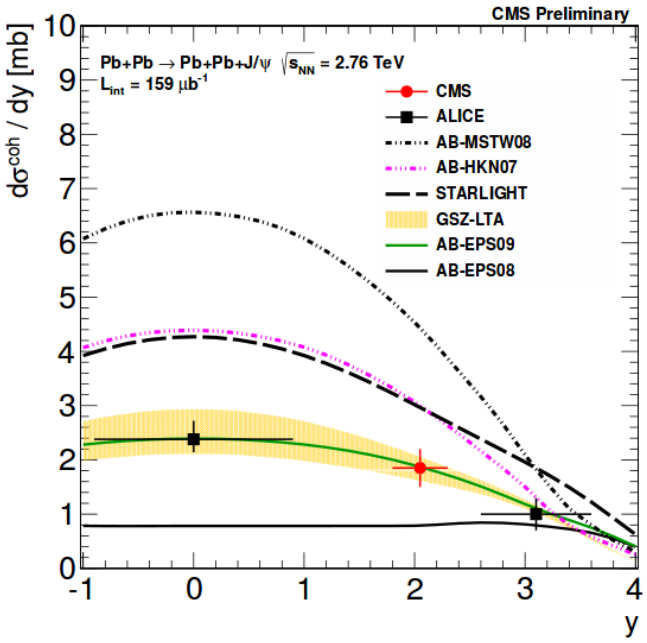

Figure 6.6: The differential cross section of the J/ψ at CMS. Taken from [81].

[1] The GSZ-LTA model was improved with ALICE results before being compared to CMS data.

Chapter 7

Analysis of the coherent ψ(2S) vector meson photoproduction with Run2 data

This analysis was done for the Pb-Pb collisions at $\sqrt{s_{NN}} = 5.02$ TeV at ALICE for the period LHC15o and Lego trains (reconstruction passes): 99 (pass1_1), 100 (pass1_pidfix), 101 (pass2_lowIR). We analyse the decay channel $\psi(2S) \to \pi^-\pi^+ J/\psi$, where $J/\psi \to \mu^-\mu^+$.

7.1 Global event selection

This analysis was performed at mid-rapidity $|y| < 0.9$ using ITS, TPC, V0, AD and ZDC detectors.

7.1.1 Trigger CCUP8

Events were triggered by the central barrel UPC trigger class CCUP8-B. Its definition is as following.

L0 trigger inputs of CCUP8-B = *0VBA *0VBC *0UBA *0UBC 0STP 0OMU;

- * = negation.
- 0VBA = signal in V0A in BB window.
- 0VBC = signal in V0C in BB window.
- 0UBA = signal in ADA in BB window.
- 0UBC = signal in ADC in BB window.
- 0STP = SPD topological trigger; at least two tracks back-to-back in azimuth.
- 0OMU = Between 2 and 6 TOF pad triggered with at least to pads in a back-to-back topology in azimuth.

The trains ran over 1.453603×10^7 triggers. The train preselected events with 4 tracks (defined by Filterbit 0). After the preselection we obtained 1.280281×10^6 events.

7.1.2 Cut for bad runs

The whole list of runs over which the trains ran is

244975 244980 244982 244983 245061 245064 245066 245068 245145 245146 245148 245151 245152 245231 245232 245233 245259 245343 245345 245346 245347 245349 245353 245396 245397 245401 245407 245409 245410 245411 245439 245441 245446 245450 245452 245453 245454 245496 245497 245501 245504 245505 245507 245535 245540 245542 245543 245544 245545 245554 245683 245692 245700 245702 245705 245729 245731 245738 245752 245759 245766 245775 245785 245793 245829 245831 245833 245923 245949 245952 245954 245963 246001 246003 246012 246036 246037 246042 246048 246049 246052 246053 246087 246089 246113 246115 246148 246151 246152 246153 246178 246180 246181 246182 246185 246217 246222 246225 246271 246272 246275 246276 246390 246391 246392 246424 246428 246431 246434 246487 246488 246493 246495 246540 246543 246553 246567 246568 246575 246583 246648 246671 246675 246676 246750 246751 246757 246758 246759 246760 246763 246765 246766 246804 246805 246807 246808 246809 246810 246844 246845 246846 246847 246851 246855 246858 246859 246864 246865 246867 246871 246928 246930 246937 246942 246945 246948 246949 246980 246982 246984 246989 246991 246994

Later on, it was discover that some of these runs did not have the quality standards required for the analysis and were rejected. The detector with problems is specified along with the runs that were rejected for this reason:

- ZDC: 245061, 245148, 246553, 246575, 246583, 246648, 246671
- TPC: 246858, 246859, 246864, 246540, 246543, 246567, 246568, 245233
- ITS: 246949
- AD: 246390, 246391, 246392
- TOF: 246980, 246928, 246428, 245738, 245700, 245452, 245439
- No UPC triggers: 246870

7.1.3 AD and V0 vetoes

After rejecting bad runs we apply UPC Trigger CCUP8-B and we provide the offline decision concerning AD, V0 and ZDC detectors. Since UPC has only the decay products of the ψ(2S) measured at mid-rapidity, the event should have no activity at forward rapidities. This is implementing vetoing activity in V0 and AD. Thus another requirement is that the AD and V0 detectors have to be empty. Although, as can be seen from the definition of the trigger CCUP8-B, there is veto for V0 and AD detector, we use these cuts again. The reason for repeating this requirement is that the V0 and AD detectors have the maximum time window 14 ns. During the data-taking for Pb-Pb collisions there was charge range larger than this time of electronics thus the V0 was setup to cover all high charges and to miss low charges. AD was set up in opposite way, it was covering all low charges and missing high charges. In other words this feature means that the V0 detector was only vetoing the high multiplicity hadronic events and the AD detector was vetoing the low multiplicity hadronic events. This can be corrected by adding the cut for V0 and AD as an offline decision. This feature can be seen in Figure 7.1 and Figure 7.2. In Figure 7.1 is depicted the AD and V0 decision after applying trigger CCUP8-B and also after rejecting bad runs which are written above. The definition of the decision which is seen in these two figures is as following:

- Region 0-1: Empty V0 and AD detectors.

- Region 1-2: Collision of beams; also denoted as Beam-Beam (BB).
- Region 2-3: Collision of beam gas; also denoted as Beam-Gas (BG).
- Region 3-4: Denoted as fake; no signal neither from beam-beam nor from beam-gas interactions.

In the next Figure 7.2 is depicted the correlation of these decisions shown in the previous figure.

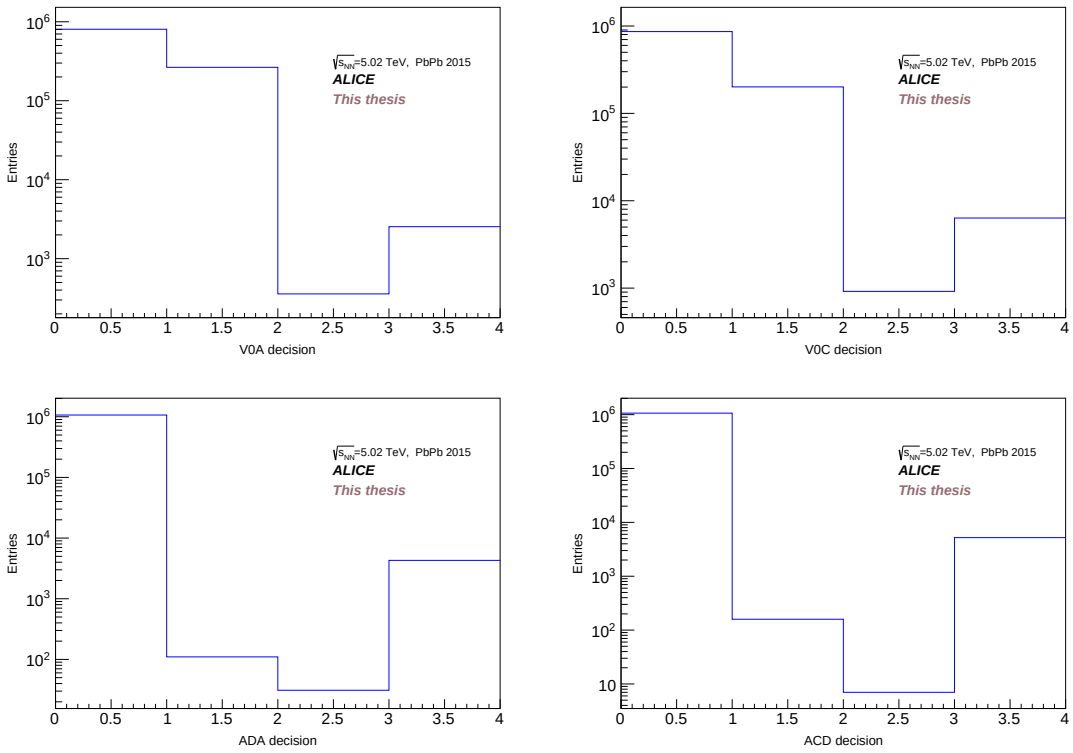

Figure 7.1: The V0, AD decisions after cuts 1 and 2, see Table 7.1.

As can be seen, it is important to repeat the requirement for AD and V0 decisions to be empty.

7.1.4 Selection criteria using the ZDC

After that we study the distribution of the ZDC time. In Figure 7.3 (up) is shown the distribution of ZDCA and ZDCC time with corresponding cuts (red and green lines, respectively). The correlation between times is in 7.3 (down) with different scale because of better visibility. As seen in the figures, the right cut for ZDC time seems to be within [-1 ns; 1 ns]. In this time region we then require to have signal from ZDC energy. Studying further the figures, we also observe, that at value of ZDC time = -999 ns there are some entries. This value is default value corresponding to timing of events without activity.

Since we are studying the coherent photoproduction of VM, some neutrons may be emitted. We allow a maximum of 6 neutrons in coherent photoproduction which corresponds to an energy of $\approx$ 15 TeV. This energy is recorded in ZDC time window [-1 ns; 1 ns]. In Figure 7.4 (up) is already applied cut for the energy in ZDC detectors and in the same figure (down) is shown the correlation of energy recorded between these two detectors.

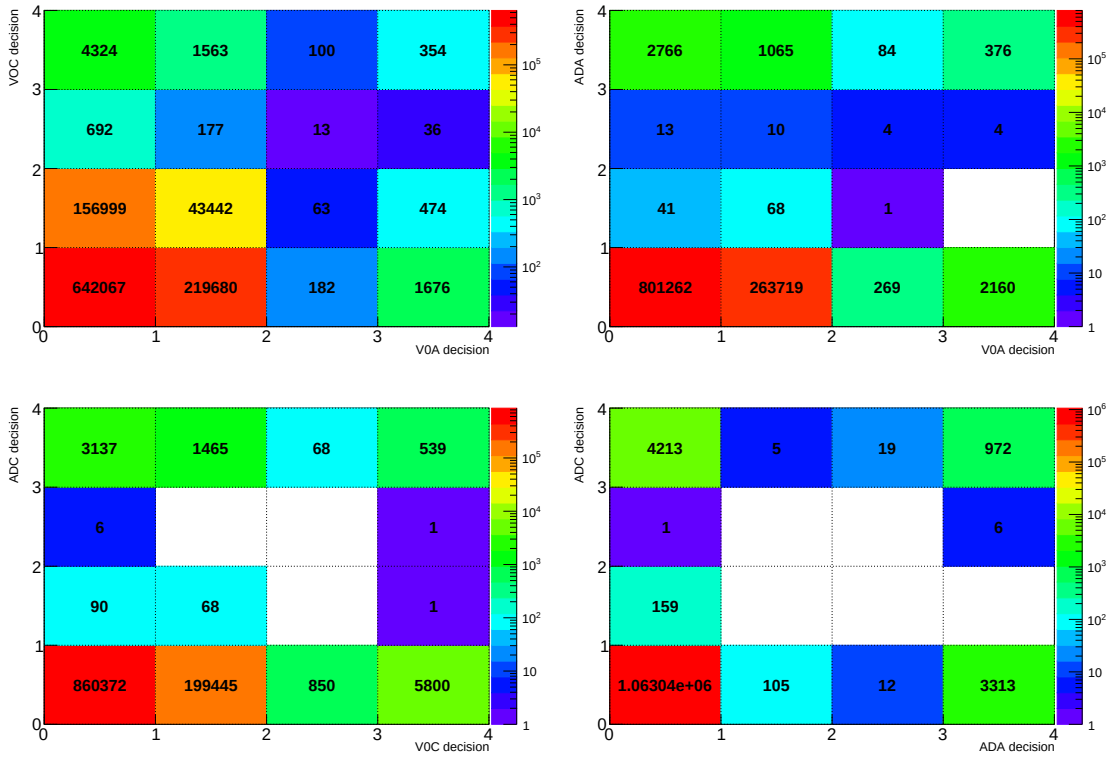

Figure 7.2: The V0, AD correlations after cuts 1 and 2, see Table 7.1.

7.2 Selection criteria related to the interaction vertex

In Figure 7.5 (left) are shown the contributors to SPD vertex already after the cut of at least 1 contributor. After this cut we study the distance between SPD vertex in z direction and primary vertex (PV) in the same direction to ensure that events became from the same vertex. In Figure 7.5 (right) we see that background contributes in distance greater than 0.3 cm and less than -0.3 cm. The green lines represent the cut.

One would expect to have exactly four tracklets, but there is a background of soft electron-positron pairs created by the strong electromagnetic fields of the incoming nuclei. This is known to produce tracklets sometimes, but it does not produce tracks, because the particles are too soft. The tail in the tracklets distribution comes mainly from these events.

7.3 The selection of tracks

To ensure that we select good tracks we apply the following cuts:

- The obvious requirement is that the track exist.
- After that we apply Filter Bit 0; Standard TPC only track cuts:
  - 50 TPC clusters as minimum.
  - The $\chi^2 < 4$ per TPC cluster.
  - Do not accept kink daughters.
  - Maximum DCA to vertex in z direction is 3.2 cm.

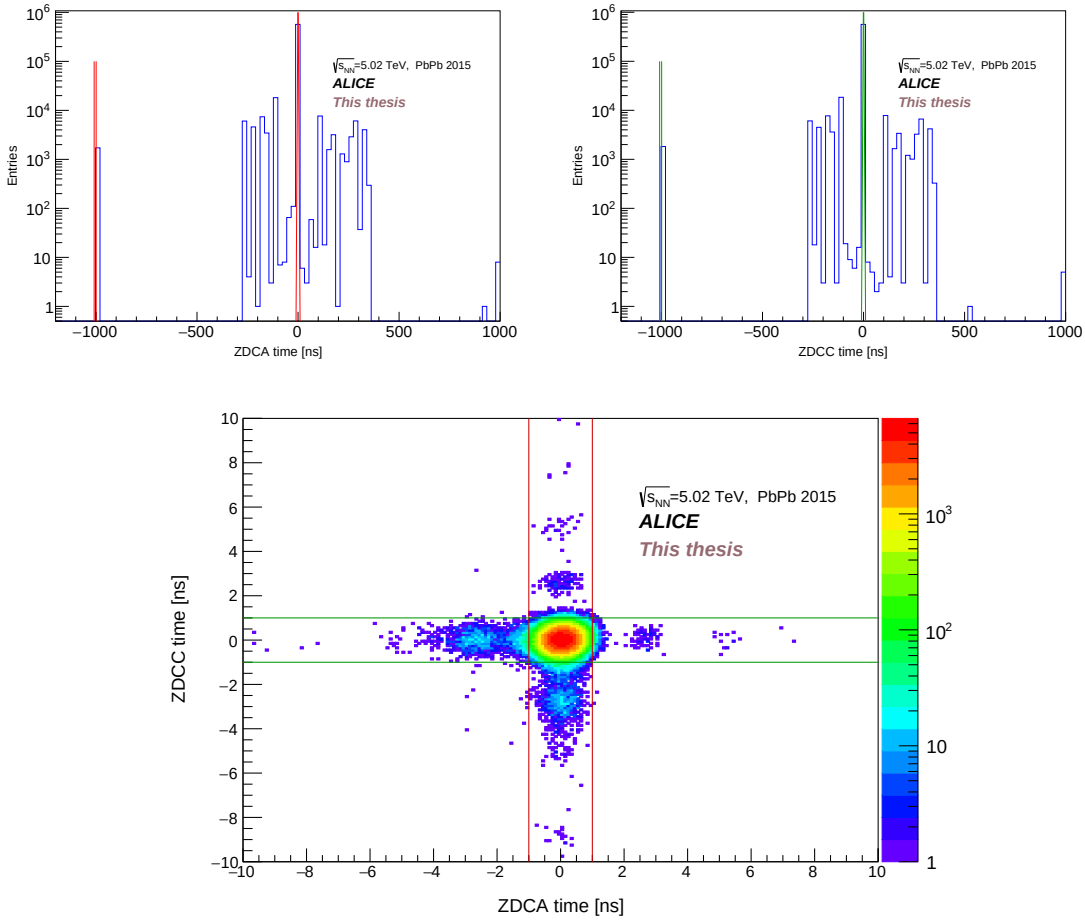

Figure 7.3: The ZDCA and ZDCC time after cuts 1, 2, 3a), 3b), 4a) and 4b), see Table 7.1. The green lines show the cut in ZDCC time, the red lines represent the cut in ZDCA time. Below is the correlation of ZDCA versus ZDCC time with these cuts depicted.

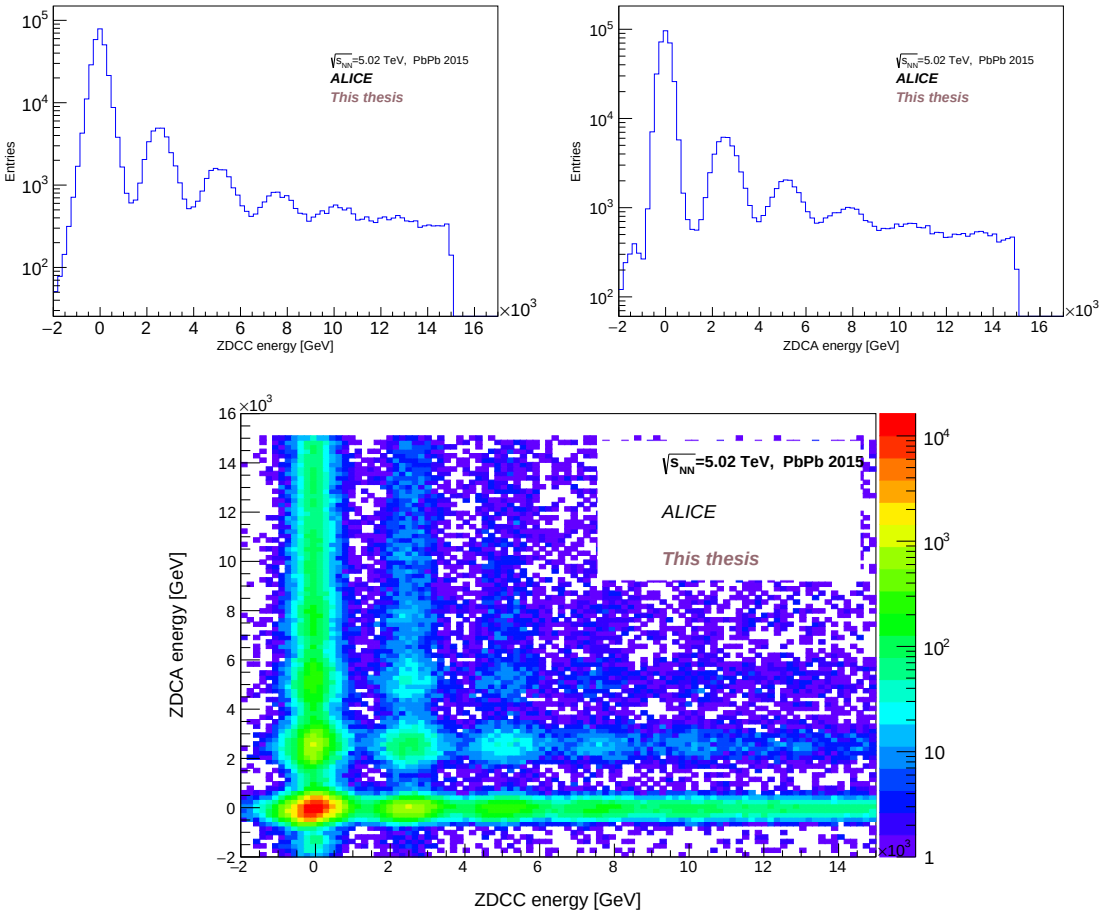

Figure 7.4: The ZDCA and ZDCC energy after cuts 1, 2, 3a), 3b), 4a), 4b), 5a-d), see Table 7.1.

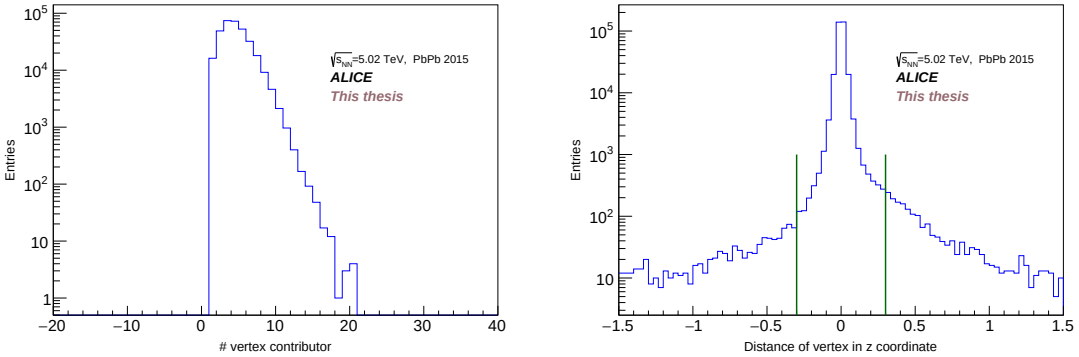

Figure 7.5: (left) The SPD vertex contributors after using cuts 1, 2, 3a), 3b), 4a), 4b), 5a-d) and 6, see Table 7.1. (right) The distance between SPD vertex in z coordinate and primary vertex in z coordinate after using cuts 1, 2, 3a), 3b), 4a), 4b), 5a), 5b), 5c) and 5d), 6. The green lines represent the cut number 7 in Table 7.1.

  - Maximum DCA to vertex in xy direction is 2.4 cm.
  - Set DCA to vertex 2D.

- TPC and ITS refit.
- At least one hit in SPD.
- The distance of closest approach DCA_z in z direction is less than 2 cm and DCA_{xy} is p_T dependent. For four tracks analysis is $|\mathrm{DCA_{xy}}| < 4(0.0182 + 0.0350/\mathrm{p_T^{1.01}})$.

Since this analysis is done for exclusive photoproduction of VM, which means that as a final state is produced only one vector meson, in this case is $\psi(2\mathrm{S}) \to \mu^+\mu^-\pi^+\pi^-$, we require exactly 4 tracks. The sum of the electric charges of the four tracks have to be zero; this is, there must be two positive and two negative tracks. In Chapter 5 we have explained that the VM has very small p_T. This in other words means that $\pi^\pm$ will have smaller p_T than that of μ's since the decay from J/ψ occur almost at rest. Thus we suppose that $\mu^\pm$ have $p_T > 1.1$ GeV/c. To distinguish muons from other particles we use TPC PID. We suppose that muons are within 4 σ[1] of the muon PID hypothesis. Although pions cannot be distinguish from muons by its energy loss, we also apply PID TPC for pions to avoid confusing them with other particles. The energy loss of muons before cut for nσ and afterwards can be seen in Figure 7.6 up left and up right, respectively. The energy loss for pions before the cut on nσ and after can be seen in the same Figure 7.6 down left and down right, respectively.

7.4 Invariant mass of $\psi(2\mathrm{S})$

Using TLorentzVector we plot the distribution of the invariant mass of the muon pair and its transverse momenta p_T, shown in Figure 7.7 left and right, respectively.

The distribution of mass of muons pair must be cut from 3.0 GeV/c^2 to 3.2 GeV/c^2 constraining the mass to the mass of J/ψ. After that adding the four momentum of the pion pair we obtain the invariant mass of $\psi(2\mathrm{S})$, Figure 7.8 (left). Since the main characteristic of the coherent photoproduction is the low p_T of the VM, we apply cut for transverse momentum as $p_T < 0.2$ GeV/c. The coherent $\psi(2\mathrm{S})$ is on the left hand side down and we select $\psi(2\mathrm{S})$ in the mass range (3.6,3.8) GeV/c^2. Down on the right can be seen the invariant mass of $\psi(2\mathrm{S})$ versus the p_T before cut for the coherence of VM. In the Figure 7.9 are shown the invariant mass of coherent $\psi(2\mathrm{S})$, SPD vertex contributors and energy in ZDC after cuts 1-18 in Table 7.1.

We summarize all the used cuts in the Table 7.1.

[1] In this context, σ is the resolution of the measurement of dE/dx at a given particle momentum. The difference between the actual dE/dx and a Bethe-like parametrization of dE/dx is measured in terms of σ to select particles compatible with a given ID hypothesis.

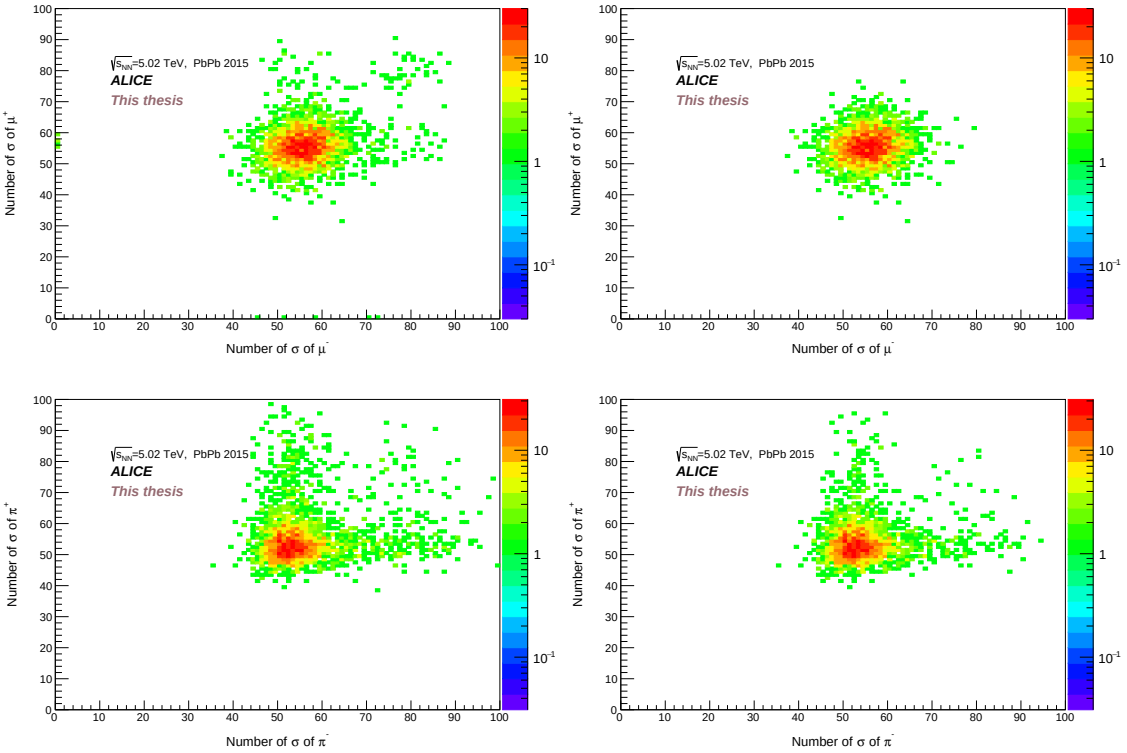

Figure 7.6: The TPC PID of μ before cut 11 (up left) and after cuts 1-11 (up right) and TPC PID π before cut 12 (down left) and after cut 1-12 (down right), see Table 7.1.

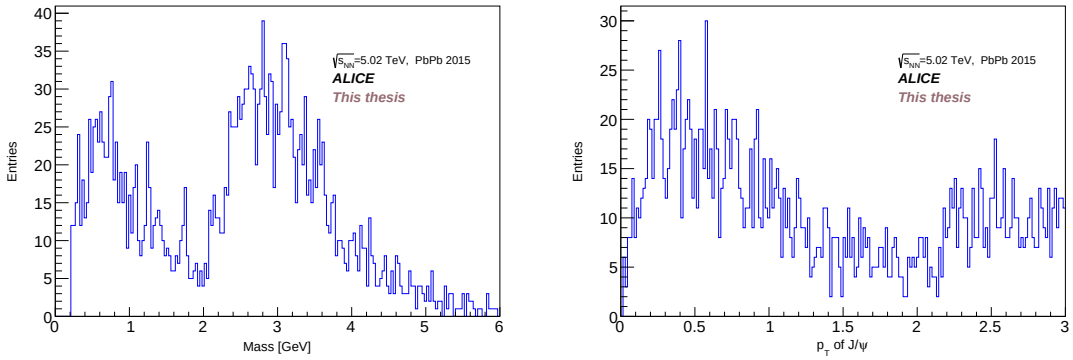

Figure 7.7: The invariant mass of muon pairs (left) after cuts 1-14 and the p_T of this pair after cuts 1-14, see Table 7.1.

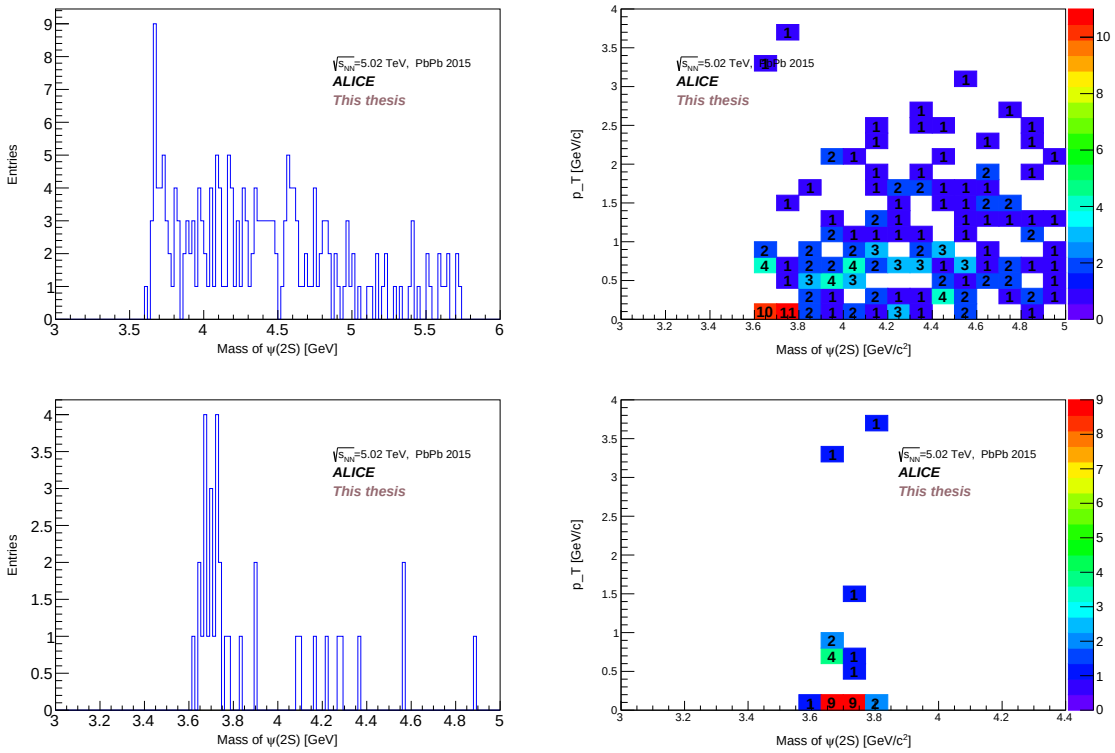

Figure 7.8: The invariant mass of ψ(2S) candidates (up left) and the mass vs. p_T of ψ(2S) (up right) after cuts 1-15, see Table 7.1. Below on the left is the coherent ψ(2S) yield and on the right is the mass of ψ(2S) vs. its p_T after cuts 1-16 from Table 7.1.

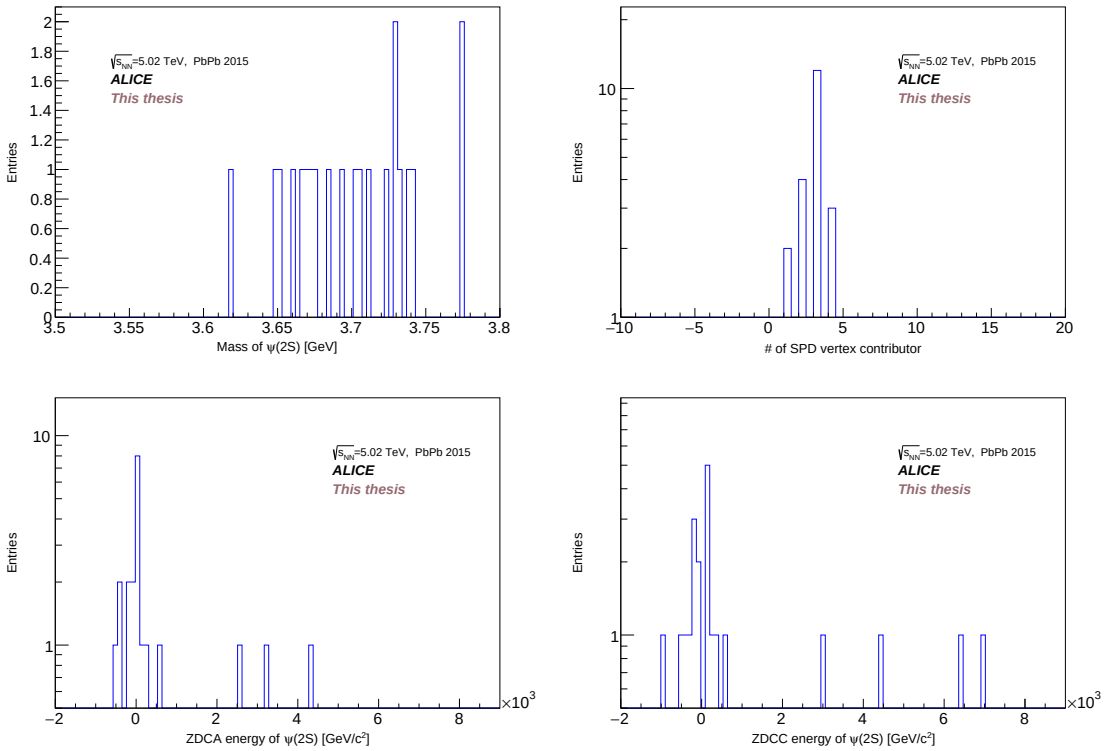

Figure 7.9: (up left) The invariant mass of ψ(2S) after cuts 1-17. (up right) The SPD vertex contributor after cuts 1-17. (Down left) the energy in ZDCA and (down right) the energy in ZDCC after cuts 1-17. For markers of cuts see Table 7.1.

Marker for cut	Cut	Selected events
	Analyzed triggers	1.453603×10^7
	'Train' preselection	1.280281×10^6
1	Bad runs rejected	1098282
2	CCUP8	1071842
3a	ADA empty	1067410
3b	ADC empty	1063037
4a	V0A empty	797890
4b	V0C empty	637558
5a	|ZDCAtime| < 1 ns or ZDCAtime = -999 ns	565288
5b	|ZDCCtime| < 1 ns or ZDCCtime = -999 ns	503134
5c	ZDCA energy < 15 TeV in time region [-1,1] ns	404305
5d	ZDCC energy < 15 TeV in time region [-1,1] ns	339444
6	At least 1 vertex contributors	339304
7	Distance between SPD vtx. and primary vtx.< 0.3 cm	332305
8	exactly 4 tracks	332305
9	Opposite charges of 4 tracks	192749
10a	track 1 is Good Track*	185091
10b	track 2 is Good Track*	179991
10c	track 3 is Good Track*	175085
10d	track 4 is Good Track*	169755
11	PID TPC of muon pair	2899
12	PID TPC of pion pair	2529
13	p_T $\mu^+ > 1.1$ Gev	14195
14	p_T $\mu^- > 1.1$ Gev	3067
15	Cut for mass of $3.0 < J/\psi < 3.2$ GeV/c^2	203
16	Cut for mass of $3.6 < \psi(2S) < 3.8$ GeV/c^2	32
17	Cut for $p_T < 0.2$ GeV/c of $\psi(2S)$	21

Table 7.1: Table of used cuts.

The Good Track* in Table 7.1 means cuts, which are mentioned in Subsection 7.3.

7.5 Next steps

The last line of Table 7.1 corresponds to the yield of $\psi(2S)$. One still needs to evaluate the rest of terms in the formula (6.1) to obtain a preliminary cross section. To do this, there is need of MC to compute the corrections. The MC were made available at the end of December 2016, so they could not be used for the thesis.

To estimate systematic uncertainties in the measurement one also needs to do variations in the selection.

All this work is in progress and when it is ready, the measurement will be submitted for publication to a leading scientific journal.

Chapter 8

Summary and discusion

The main purpose of the analysis described in this work was to study ultra-peripheral Pb-Pb collisions in order to investigate the behaviour of the gluon distribution of lead nuclei at small values of x.

A collision of heavy ions at an impact parameter greater than the sum of their radii occurs via the interaction of a photon with one of the heavy ions and the creation of a vector meson, which is called photoproduction. This thesis was dedicated to the study of the coherent photoproduction of a ψ(2S) in its decay channel to $\psi(2S) \rightarrow J/\psi + \pi^+\pi^-$, and subsequently $J/\psi \rightarrow \mu^+\mu^-$ at mid-rapidity (see Figure 5.3). More about the underlying physics of this studied process was presented in Chapters 2, 3 and 5 .

In Chapter 7, details of this analysis were presented. Since this process is exclusive (see more in Chapter 5), we selected exactly 4 tracks. From these tracks we then selected pairs of pions and pairs of muons. Considering the decay channel under study, these pairs have to have opposite charges. Since the process is the coherent photoproduction, the momentum of the ψ(2S) is less than 0.2 GeV, which means that the J/ψ and pions are almost back-to-back and that their p_T is very small. We supposed that the muons decaying from J/ψ will have $p_T > 1.1$ GeV. Applying the TPC PID to these tracks we identified muons from pions.

Next step was to assure that muons came from J/ψ, so we applied cut for the mass of the pair of muons to be within (3.0, 3.2) GeV/c^2. Adding the masses of pions we obtained the invariant mass of ψ(2S). Additionally, we required the p_T of ψ(2S) to be less than 0.2 GeV since it is coherent photoproduction and at the same time we cut the mass distribution to the range $3.6 < M_{\psi(2S)} < 3.8$ GeV/c^2, see Figure 7.8.

All these steps should be repeated with generated particles from Monte Carlo simulations. However, since the required files were made available only at the end of the December 2016, this will be done as a next step in the analysis. Remaining necessary information obtained from MC will be used for calculation of the cross section, see Equation (6.1). Along with repeating the measurement with a different track selection to estimate systematic uncertainties, we also plan to study other decay channels. We also compare the measurements to the existing models and thus put further constraints to some models or exclude them. All this work is in progress and when it is ready, it will be submitted for publication to a leading scientific journal.

Bibliography

[1] N. Bohr. XXXVII. on the constitution of atoms and molecules. *Philosophical Magazine Series 6*, 26(153):476–502, 1913.

[2] N. Bohr. I. on the constitution of atoms and molecules. *Philosophical Magazine Series 6*, 26(151):1–25, 1913.

[3] James Chadwick. Possible existence of a neutron. *Nature*, 129(3252):312, 1932.

[4] Murray Gell-Mann. A Schematic Model of Baryons and Mesons. *Phys. Lett.*, 8:214–215, 1964.

[5] G. D. Rochester and C. C. Butler. Evidence for the Existence of New Unstable Elementary Particles. *Nature*, 160:855–857, 1947.

[6] J. D. Bjorken and S. L. Glashow. Elementary Particles and SU(4). *Phys. Lett.*, 11:255–257, 1964.

[7] S. L. Glashow, J. Iliopoulos, and L. Maiani. Weak Interactions with Lepton-Hadron Symmetry. *Phys. Rev.*, D2:1285–1292, 1970.

[8] Burton Richter. Discovery of the psi Particles: A Personal Perspective. *SLAC Beam Line. Vol. 7, No. 11. 11/1976*, 1976.

[9] J. J. Aubert et al. Experimental Observation of a Heavy Particle J. *Phys. Rev. Lett.*, 33:1404–1406, 1974.

[10] J. E. Augustin et al. Discovery of a Narrow Resonance in e+ e- Annihilation. *Phys. Rev. Lett.*, 33:1406–1408, 1974.

[11] F. Abe et al. Observation of top quark production in $\bar{p}p$ collisions. *Phys. Rev. Lett.*, 74:2626–2631, 1995.

[12] S. W. Herb et al. Observation of a Dimuon Resonance at 9.5-GeV in 400-GeV Proton-Nucleus Collisions. *Phys. Rev. Lett.*, 39:252–255, 1977.

[13] P. A. M. Dirac. A Theory of Electrons and Protons. *Proc. Roy. Soc. Lond.*, A126:360, 1930.

[14] Paul A. M. Dirac. Quantized Singularities in the Electromagnetic Field. *Proc. Roy. Soc. Lond.*, A133:60–72, 1931.

[15] C. Patrignani et al. Review of Particle Physics. *Chin. Phys.*, C40(10):100001, 2016.

[16] V. E. Barnes et al. Observation of a Hyperon with Strangeness -3. *Phys. Rev. Lett.*, 12:204–206, 1964.

[17] W. Pauli. The Connection Between Spin and Statistics. *Phys. Rev.*, 58:716–722, 1940.

[18] Nobel lecture of pauli. `http://www.nobelprize.org/nobel_prizes/physics/laureates/1945/pauli-lecture.html`. Accessed: 2016-13-03.

[19] O. W. Greenberg. Spin and Unitary Spin Independence in a Paraquark Model of Baryons and Mesons. *Phys. Rev. Lett.*, 13:598–602, 1964.

[20] K. A. Olive et al. Review of Particle Physics. *Chin. Phys.*, C38:090001, 2014.

[21] R.C. Barrett and D.F. Jackson. *Nuclear sizes and structure*. International series of monographs on physics. Clarendon Press, 1977.

[22] Coughlan G. D., Dodd J. E., and Gripaios B. M. *The Ideas of Particle Physics*. Cambridge University Press, 2006.

[23] J. D. Bjorken. Asymptotic Sum Rules at Infinite Momentum. *Phys. Rev.*, 179:1547–1553, 1969.

[24] J. D. Bjorken and Emmanuel A. Paschos. Inelastic Electron Proton and gamma Proton Scattering, and the Structure of the Nucleon. *Phys. Rev.*, 185:1975–1982, 1969.

[25] R. P. Feynman. The behavior of hadron collisions at extreme energies. *Conf. Proc.*, C690905:237–258, 1969.

[26] C. G. Callan and David J. Gross. Crucial Test of a Theory of Currents. *Phys. Rev. Lett.*, 21:311–313, 1968.

[27] H. Fritzsch, Murray Gell-Mann, and H. Leutwyler. Advantages of the Color Octet Gluon Picture. *Phys. Lett.*, B47:365–368, 1973.

[28] H. David Politzer. Reliable Perturbative Results for Strong Interactions? *Phys. Rev. Lett.*, 30:1346–1349, 1973.

[29] David J. Gross and Frank Wilczek. Ultraviolet Behavior of Nonabelian Gauge Theories. *Phys. Rev. Lett.*, 30:1343–1346, 1973.

[30] M. Klein and R. Yoshida. Collider Physics at HERA. *Prog. Part. Nucl. Phys.*, 61:343–393, 2008.

[31] H. Abramowicz et al. Combination of measurements of inclusive deep inelastic $e^{\pm}p$ scattering cross sections and QCD analysis of HERA data. *Eur. Phys. J.*, C75(12):580, 2015.

[32] V.N. Gribov and L.N. Lipatov. Deep inelastic e p scattering in perturbation theory. *Sov.J.Nucl.Phys.*, 15:438–450, 1972.

[33] Guido Altarelli and G. Parisi. Asymptotic Freedom in Parton Language. *Nucl.Phys.*, B126:298, 1977.

[34] Yuri L. Dokshitzer. Calculation of the Structure Functions for Deep Inelastic Scattering and e+ e- Annihilation by Perturbation Theory in Quantum Chromodynamics. *Sov.Phys.JETP*, 46:641–653, 1977.

[35] Victor S. Fadin, E.A. Kuraev, and L.N. Lipatov. On the Pomeranchuk Singularity in Asymptotically Free Theories. *Phys.Lett.*, B60:50–52, 1975.

[36] L.N. Lipatov. Reggeization of the Vector Meson and the Vacuum Singularity in Nonabelian Gauge Theories. *Sov.J.Nucl.Phys.*, 23:338–345, 1976.

[37] E. A. Kuraev, L. N. Lipatov, and Victor S. Fadin. Multi - Reggeon Processes in the Yang-Mills Theory. *Sov.Phys.JETP*, 44:443–450, 1976.

[38] E.A. Kuraev, L.N. Lipatov, and Victor S. Fadin. The Pomeranchuk Singularity in Nonabelian Gauge Theories. *Sov.Phys.JETP*, 45:199–204, 1977.

[39] I.I. Balitsky and L.N. Lipatov. The Pomeranchuk Singularity in Quantum Chromodynamics. *Sov.J.Nucl.Phys.*, 28:822–829, 1978.

[40] N. Armesto. Introduction to low x physics and saturation. *Acta Phys. Polon.*, B35:213–222, 2004.

[41] Yuri V. Kovchegov. Small x F(2) structure function of a nucleus including multiple pomeron exchanges. *Phys.Rev.*, D60:034008, 1999.

[42] Yuri V. Kovchegov. Unitarization of the BFKL pomeron on a nucleus. *Phys.Rev.*, D61:074018, 2000.

[43] I. Balitsky. Operator expansion for high-energy scattering. *Nucl.Phys.*, B463:99–160, 1996.

[44] Ian Balitsky. Factorization and high-energy effective action. *Phys.Rev.*, D60:014020, 1999.

[45] I. Balitsky. Factorization for high-energy scattering. *Phys.Rev.Lett.*, 81:2024–2027, 1998.

[46] Ian Balitsky. Effective field theory for the small x evolution. *Phys.Lett.*, B518:235–242, 2001.

[47] A. Accardi et al. Electron Ion Collider: The Next QCD Frontier - Understanding the glue that binds us all. 2012.

[48] Nestor Armesto. Nuclear shadowing. *J. Phys.*, G32:R367–R394, 2006.

[49] J. J. Aubert et al. The ratio of the nucleon structure functions $F2_n$ for iron and deuterium. *Phys. Lett.*, B123:275–278, 1983.

[50] V. Guzey, M. Strikman, and M. Zhalov. Accessing transverse nucleon and gluon distributions in heavy nuclei using coherent vector meson photoproduction at high energies in ion ultraperipheral collisions. 2016.

[51] The establishment of CERN. `http://www.chipp.ch/chipp-meet-symposiumCERN50.html`. Accessed: 2016-10-03.

[52] The scheme of LEP and LHC. `http://timeline.web.cern.ch/timelines/The-Large-Hadron-Collider`. Accessed: 2016-07-03.

[53] Lyndon Evans and Philip Bryant. LHC Machine. *JINST*, 3:S08001, 2008.

[54] C Lefevre. LHC: the guide (Czech version). CERN Guide du LHC (Czech version). Sep 2008.

[55] The scheme of the complex of CERN. https://commons.wikimedia.org/wiki/File:Cern-accelerator-complex.svg. Accessed: 2016-07-03.

[56] History of ALICE. http://alice20.web.cern.ch/alice20/#banner. Accessed: 2016-13-03.

[57] 20 years of ALICE detector. http://alice20.web.cern.ch/alice20/#year_2004. Accessed: 2016-13-05.

[58] K. Aamodt et al. The ALICE experiment at the CERN LHC. *JINST*, 3:S08002, 2008.

[59] Betty Bezverkhny Abelev et al. Performance of the ALICE Experiment at the CERN LHC. *Int. J. Mod. Phys.*, A29:1430044, 2014.

[60] 3D ALICE schematic - with description. https://aliceinfo.cern.ch/Figure/node/3400. Accessed: 2016-11-05.

[61] P Cortese et al. ALICE: Physics performance report, volume I. *J. Phys.*, G30:1517–1763, 2004.

[62] P Cortese et al. ALICE: Physics performance report, volume II. *J. Phys.*, G32:1295–2040, 2006.

[63] F. Antinori. The Alice inner tracking system. *Nucl. Instrum. Meth.*, A511:215–220, 2003.

[64] ITS sketch. http://aliceinfo.cern.ch/ITSUpgrade/. Accessed: 2016-28-05.

[65] Andrea Rossi. *Charm production in proton-proton collisions at the LHC with the ALICE detector. Produzione di charm in collisioni protone-protone al Large Hadron Collider con il rivelatore ALICE.* PhD thesis, Trieste U., 2010.

[66] Andrea Agostinelli. *Vector meson photoproduction in ultra-peripheral heavy ion collisions with ALICE at the LHC.* PhD thesis, Bologne U., 2014.

[67] Christian Lippmann. Particle identification. *Nucl. Instrum. Meth.*, A666:148–172, 2012.

[68] The particle identification on TOF. http://aliceinfo.cern.ch/ArtSubmission/node/1562. Accessed: 2016-28-05.

[69] Time of flight. http://cerncourier.com/cws/article/cern/54018. Accessed: 2016-29-05.

[70] E. Abbas et al. Performance of the ALICE VZERO system. *JINST*, 8:P10016, 2013.

[71] K. Oyama. Reference cross section measurements with ALICE in pp and Pb-Pb collisions at LHC. In *LHC Lumi Days 2012 Geneva, Switzerland, February 29-March 1, 2012*, 2013.

[72] WLS fibres of the v0. http://aliceinfo.cern.ch/ArtSubmission/node/595. Accessed: 2016-28-05.

[73] The scheme of the spectators. http://cerncourier.com/cws/article/cern/53089. Accessed: 2016-06-03.

[74] J Daniel Tapia Takaki and O Villalobos Baillie. *Physics performance studies for the ALICE experiment at the CERN LHC*. PhD thesis, Birmingham U., Birmingham, UK, 2008. Presented on 27 Jan 2008.

[75] Biswarup Paul and Sukalyan Chattopadhyay. *Charmonium studies at LHC energies using the ALICE Muon Spectrometer*. PhD thesis, HBNI, Mumbai, May 2015. Presented 15 Sep 2015.

[76] MonALISA. `http://alimonitor.cern.ch/map.jsp`. Accessed: 2016-12-31.

[77] S. Afanasiev et al. Photoproduction of J/psi and of high mass e+e- in ultra-peripheral Au+Au collisions at s**(1/2) = 200-GeV. *Phys. Lett.*, B679:321–329, 2009.

[78] E. Abbas et al. Charmonium and e^+e^- pair photoproduction at mid-rapidity in ultra-peripheral Pb-Pb collisions at $\sqrt{s_{\rm NN}}$=2.76 TeV. *Eur. Phys. J.*, C73(11):2617, 2013.

[79] Betty Abelev et al. Coherent J/ψ photoproduction in ultra-peripheral Pb-Pb collisions at $\sqrt{s_{NN}} = 2.76$ TeV. *Phys. Lett.*, B718:1273–1283, 2013.

[80] Jaroslav Adam et al. Coherent ψ(2s) photo-production in ultra-peripheral pb pb collisions at $\sqrt{s}_{\rm nn} = 2.76$ tev. *Phys. Lett.*, B751:358–370, 2015.

[81] CMS Collaboration. Photoproduction of the coherent J/ψ accompanied by the forward neutron emission in ultra-peripheral PbPb collisions at 2.76 TeV. 2014.